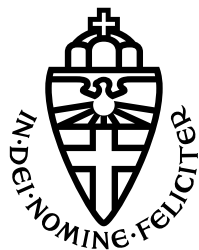


RADBOUD UNIVERSITY NIJMEGEN



FACULTY OF SCIENCE

Low frequency radio astronomy in Lunar orbit

CHANG'E 7 SCIENCE PROPOSAL

THESIS MSc ASTROPHYSICS

Author: Ronald BOUMA *Supervisor:* prof. dr. Marc KLEIN-WOLT
Second reader: Prof. Dr. Jörg R. Hörandel

May 25, 2023

Contents

1	Introduction	3
2	Mission context	5
2.1	Chang'e 7	5
2.2	Proposal of the general architecture	5
3	Constraints on observation of Ultra-low frequency radio emission	7
3.1	Diffraction limit	7
3.2	Lunar Ionosphere	8
3.3	Scintillation	8
3.4	Depolarization	8
3.5	Background emission	9
3.6	Smearing	10
3.7	Synchronisation and localization	11
4	Scientific objectives	13
4.1	Ultra low frequency sky map	13
4.2	Active Galactic Nuclei, feedback and fossil radio galaxies	14
4.2.1	Low frequency spectrum	14
4.2.2	Dying and fossil radio galaxies	15
4.3	Cosmology	16
4.4	Planetary and solar emission	16
4.4.1	Coronal mass ejections	17
4.4.2	Planetary emission	18
4.5	Exoplanet and dwarf emissions	19
4.6	ISM probing	21
4.7	Origin of cosmic rays	21
4.8	Lunar Ionosphere probing	22
5	Lunar orbit	23
5.1	Stable orbit	23
5.2	Δv requirements	24
6	Simulation setup	27
6.1	sidestepping the w problem	27
6.2	Sky map	29
6.3	single source PSF	30
7	Simulations	34
7.1	Setup	34
7.1.1	Input model	34
7.1.2	Noise	36
7.1.3	Orbit selection and surface station effects	37
7.2	Results	38
7.2.1	Full sky image	39
7.2.2	Noise analysis	44
7.2.3	Angular noise spectrum	46
7.3	Cleaned results	50

8 Requirements	54
8.1 Observing bandwidth and resolution	54
8.2 Data rate and down-link	55
8.3 System noise	56
8.4 Localization	56
8.5 Antenna length	57
8.6 Δv	57
9 Conclusion	58
10 Suggestions for further work	58
10.1 Smearing	58
10.2 Satellite orientation effects	58
10.3 Very low frequency	59
10.4 Synchronisation and localization	59
10.5 Calibration	59
10.6 Stationkeeping and disposal	60
A Code	65

1 Introduction

With the advent of renewed interest in performing lunar missions by multiple institutions certain scientific area's of interest are opening up. One of these scientific areas of interest is very low-frequency radio astronomy [1]. Since the Earth's ionosphere scatters radio waves increasingly at lower frequency the area of the electromagnetic spectrum below around 30 MHz remains woefully understudied [2]. Some attempts are being made, for example LOFAR is actively studying this region of the spectrum but ionospheric interference makes observations dependant on the state of the upper atmosphere which makes long duration studies difficult and less reliable at the very low end [3]. The lunar neighborhood, in contrast to the surface of the Earth, provides an excellent location to study these frequencies. And given the number of missions set to leave for this area of space the opportunities that are available to do just that are increasing. And even modest systems such as the one proposed here can perform useful and novel scientific observations.

This work will focus on the possibilities provided by the Chinese Chang'e 7 mission. This mission is set to have a lander touch down on the surface of the Moon as well as providing capabilities for multiple orbiting stations. This allows the use of (limited) interferometry to be performed on the very low end of the electromagnetic frequency spectrum. Although the work is tailored to this specific setup it is easily transferable to any other similar missions that is composed of a combination of landed (on the lunar surface) and orbiting elements.;

In this thesis the constraints placed on such a system will first be looked at (chapter 3). The nature of these low frequencies introduces some difficulties on performing the observations that are not always present for higher frequencies, such as scintillation of the interplanetary medium.

Then some of the scientific possibilities for such a system are discussed (chapter 4) Not all the scientific objectives for very low frequency observations can be achieved by the limited system as is proposed here but there are several where even the limited collecting area of this limited system can be of great scientific value. Since the goal of this thesis is showing that such a system can be used for the gathering of useful scientific data some science cases will be simulated. These simulations will focus mainly on some of the easier to achieve scientific objectives. But in order to perform these simulations some extra inputs must first be distilled and are therefore discussed first. the fact that some elements of the system will be orbiting requires some decisions such as orbital parameters (chapter 5) and the problem of the w term in standard radio astronomy (chapter 6.1). When these elements are known as well as how the reconstruction of useful sky data can be reconstructed from the observations the set up for the simulations will be complete.

The results of the simulations will show that the modest three elements interferometry system can perform the observations required for the distilling of useful scientific data for the cases of making a detailed very low frequency sky map, as well as identification and study of sources such as fossil radio galaxies (7).

The results will show that the system proposed will need a large amount of observing time, on the order of 4 or more years, to identify sources at the lowest frequencies (10 Mhz) with a strength of approximately 1 Jansky. This amount of observing time however is certainly doable by choosing orbits and supporting systems correctly.

2 Mission context

2.1 Chang'e 7

The Chinese National Space Administration (CNSA) has been steadily moving forward with their goal of lunar exploration in preparation for manned missions to (tentatively) take place in the 2030's. The Chang'e program has so far had several successful missions to lunar orbit and the surface. The CNSA has collaborated, and is planning to collaborate, with international partners to develop and deploy scientific experiments onboard the hardware launched by the Chinese. Most notably for this work the Chang'e 4 mission carried the 'Netherlands-China Low-Frequency Explorer' (NCLE) onboard the Chang'e 4 orbiter. This experiment built and designed by Radboud University in collaboration with Astron and ISISpace, is considered a pathfinder mission for future low frequency radio astronomy done from the lunar neighborhood.

The mission objective for the Chang'e 7 is to survey the Moon from a polar orbit and to have a lander on or near the lunar south pole to look for water (ice) on the surface. In addition to the main orbiter and lander a (or several) smaller probe is to be released from the main orbiter [4].

This mission provides a unique opportunity to expand upon the NCLE pathfinder mission to do low frequency long baseline radio interferometry from lunar orbit and the surface.

It is also not the only mission planned for lunar orbit, with the Artemis program becoming operational in the coming years the amount of launches to this area of space is expected to increase dramatically [5].

The scale of the baselines possible in lunar orbit and the radio quiet environment allows for data to be gathered on astronomical sources that so far have not been studied in any great detail.

Though this work is focused on the Chang'e 7 mission context it can also be used in any other mission where more than one orbital elements are available plus optional ground elements.

2.2 Proposal of the general architecture

The very low end of the radio spectrum, below a frequency of 30MHz is extremely hard to measure from the surface of the Earth. The atmosphere blocks and scatters these low frequencies in such a way that it is hard to determine the origin of these emissions [6]. These effects scale as ν^{-2} which makes them a big issue at the lowest frequencies. In an Earth orbit many of these effects will be muted to a degree but a Earth orbiting system would still have to deal with a rather large source of noise, namely the Earth. Lunar orbit and surface provides a radio quiet environment without atmospheric effects present. An environment that is also reasonably within reach.

In order to perform the low frequency radio astronomy experiments the added experiments are relatively minor in terms of added complexity. The main components would be omnidirectional antenna's (simple dipoles) on each of the three components of the mission (lander, service module and small released satellite). This relatively simple setup allows for measurements of the low frequency spectrum at a resolution and with a time span that has so far never been done.

In this work it is assumed that there is one ground (lunar surface) station at or near the lunar south pole, along with one orbiter that is in a near polar orbit to allow for full mapping of the lunar surface (likely inclined 86 degrees to reduce gravitational effects

that will push the orbiter into a different orbit), along with a second orbiter that has some potential to be moved into a separate orbit. Each of these elements is assumed to have identical characteristics for the collection of radio waves.

3 Constraints on observation of Ultra-low frequency radio emission

Due to the scattering of radio waves by free electrons there is a cut-off frequency below which we cannot look with radio telescopes from the Earth's surface. The plasma frequency of the Earth's ionosphere is typically around 10 MHz. Below this frequency observations done from the Earth's surface are essentially blind in the radio spectrum. Of course there are other effects such as scintillation that cause images to be distorted. These all contribute to being unable to do accurate radio astronomy below about 30 MHz.

In lunar orbit (and on the surface) these factors are not present, or at the very least likely to only be problem at frequencies far lower than they are on Earth. The interplanetary and interstellar medium have plasma frequencies in the order of several tens of kilohertz [7].

This does not mean however that there are no constraints on the observations that can be made with the setup that is proposed here.

3.1 Diffraction limit

The primary limiting factor for most Earth based radio observatories for the achievable resolution is the diffraction limit. This limit is caused by inherent properties of light and can therefore not be circumvented. The issue arises that the dark ridges of a source starts to overlap with another source causing interference between the two sources present, this effect makes it impossible to differentiate between the separate sources which makes it appear as a single source instead. It depends on the wavelength of the light and the size of the aperture. In radio astronomy however by using multiple simultaneous measurements from different antenna's we can replace the size of the aperture with the size of the spacing between the different antennas:

$$\Theta = 1.22 \frac{\lambda}{B} \quad (1)$$

Where Θ is the maximum possible angular resolving power (how close two sources can be together and still be counted as separate) in radians, λ is the wavelength and B is the length of the baseline available (distance between two measurements). Assuming some typical numbers for an interferometer in orbit around the Moon we take for a baseline around $1700 * 10^3$ meters (approximately the radius of the Moon, and therefore about the average distance between the antenna's) we get for the best case angular resolution:

- For 1 MHz ($\lambda = 299.8$ meters): 36.4"
- For 5 MHz ($\lambda = 59.958$ meters): 7.3"
- For 10 MHz ($\lambda = 29.98$ meters): 3.6"

For the frequencies we are interested in the diffraction limit imposes a hard lower limit for the best achievable resolving power of such a system. This will limit the ability of the system to identify separate individual sources, however larger structures that are made up by individual sources are still detectable.

One could achieve a better resolution by for example using only longer baselines in the calculation, achieved by boosting the satellites into a higher orbit for example. However

as we will see other effects will impose a much stricter lower limit. Therefore this lower limit represent only a theoretical lower limit that is likely not achievable.

3.2 Lunar Ionosphere

The primary factor of why very low frequency observation from the Earth is difficult is the effect of the Earth's atmosphere. The atmosphere blocks, diffracts and scatters these lower frequencies. Although quiet periods in the atmosphere do happen they are fairly infrequent which limits observation times for these frequencies.

The Moon however is not entirely devoid of an atmosphere and ionosphere. They are however far less dense and it does not reach as high up from the surface.

For the day side of the Moon we have data that suggests that the maximum plasma frequency on the surface is about 1MHz with a low of 0.2MHz [8].

There is however very little data on the extent on the lunar ionosphere as well as limited data available for the night side of the Moon. It is assumed that the values for the plasma frequency are much lower but no confirmation of these assumptions have been given.

Since these constrains are not well known due to being not accurately measured this work has assumed that an absolute lower limit of observation (from the surface) of 0.5MHz is reasonable.

3.3 Scintillation

The interplanetary and interstellar medium have electron densities which cause electromagnetic waves to be refracted. The effect of this scintillation causes an effect on the observations that is similar in effect to seeing caused by turbulence in the atmosphere. The intensity of the incoming radiation is not diminished but instead spread out over a larger angle than it was originally emitted. This effectively reduces the angular resolution that can be achieved on the sky. Sources close to one another will overlap in the observation. This effect is highly dependent on the frequency of the radiation. The effect is given in equation 2 [9] [10]. Due to the different electron densities present these must be split between scintillation coming from the interplanetary and interstellar medium (IPM and ISM respectively). The worst case scenarios are given by:

$$\Theta_{ISM} \approx \frac{30'}{\left(\frac{\nu}{MHz}\right)^{2.2} \sqrt{\sin(b)}} \quad (2a)$$

$$\Theta_{IPM} \approx \frac{100'}{\left(\frac{\nu}{MHz}\right)^2} \quad (2b)$$

In this equation Θ is the angular scattering size, ν is the frequency and b is the galactic latitude. the power index of 2.2 in the ISM arises from turbulence present in the electron density and the equation is valid for $b > 15^\circ$. For angles smaller than this a modified equation is used where $\Theta_{ISM} \approx \frac{22'}{(\nu/MHz)^{2.2}}$ [11].

In figure 1 the effects of scintillation and the diffraction limit are plotted together. It is clear that for the frequency of interest the interplanetary scintillation provides the absolute limit for the theoretical resolution of the observations.

3.4 Depolarization

Another effect of the IPM and ISM is that at these frequencies linear polarization is greatly affected. These regions contain both free electrons and a magnetic field leading

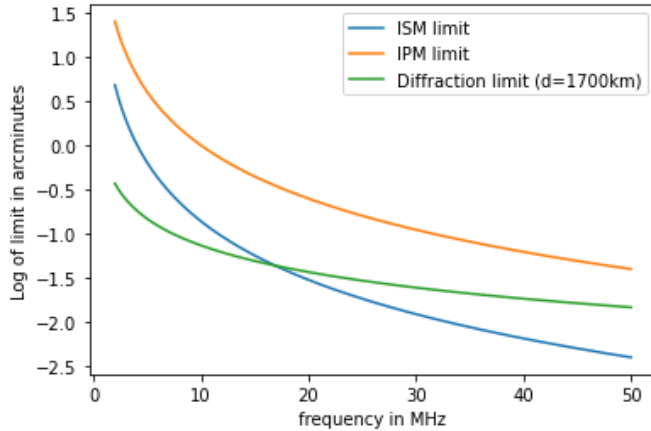


Figure 1: The theoretical limiting factors on the angular resolutions plotted together, for the ISM the modified version is used for viewing close to the galactic plane

to Faraday rotation. The RMS that such a region has on the polarization is [12]:

$$\Delta\Psi_{RMS} = 2.6 \times 10^{-13} \lambda^2 \Delta N_e a B \sqrt{\frac{L}{a}} \quad (3)$$

Where $\Delta\Psi_{RMS}$ is the root mean square of the rotation in radians, λ is the wavelength of the radiation, ΔN_e is the over-density of electrons (the increase in electron density compared to the region before it and after it), a is the size of the electron dense region, B is the magnetic field along the line of light and L is the free path length in the region. using some standard values and sizes for the ISM, $a = 10^{-3}$ pc $N_e = 0.3 \times 10^5 \text{ m}^{-3}$ and $B = 0.5 \text{ nT}$, we arrive at a an RMS of about 1 radian at a frequency of 1 MHz per cell. Since these cells are scattered all over the ISM this effect leads to complete depolarization on (astronomically speaking) short distances.

The IPM's effect on polarization is mostly driven by the stellar wind that emits charged particles and is therefore more subject to instantaneous changes in solar activity.

On the other hand circular polarization is not affected in any meaningful way [10]. This discrepancy can be beneficial to certain kinds of observations, since some astronomical sources (exoplanets for example) emit almost exclusively circularly polarized radio emissions. These sources can therefore be studied with a higher degree of accuracy than linear polarized sources by filtering for only circular polarization.

3.5 Background emission

At the low frequencies that are of interest the backgrounds emissions are dominated by synchrotron radiation. This causes a lot of noise to be present at low frequencies. The background/Foreground emissions do form a area of interest in of itself when making a sky map, but it does interfere when trying to study specific sources of interest, in which case it can be categorized as noise for that specific purpose.

This noise can be quantified by the sky temperature. The Sky temperature is highly dependent on frequency. The sky temperatures of interest are estimated to be[11]:

$$T_{sky} = \begin{cases} 16.3 \times 10^6 K \left(\frac{\nu}{2\text{MHz}}\right)^{-2.35}, & \text{at } \nu \geq 2\text{MHz} \\ 16.3 \times 10^6 K \left(\frac{\nu}{2\text{MHz}}\right)^{-0.3}, & \text{at } \nu < 2\text{MHz} \end{cases} \quad (4)$$

These sky temperatures especially at frequencies lower than about 15 MHz leads to extremely high sky temperatures. Therefore in order to identify sources located within these emissions many independent measurements would have to be performed.

3.6 Smearing

Integration time is an important part of reducing the amount of noise in any intermetric measurement. The same can be achieved by stacking a multiple of measurements (see section 6.1). However making a large number of measurements in quick succession requires additional features put upon the system requirements, for example data storage and data link rates. Therefore a reduction of the amount of measurements in a given time frame would be preferable.

The problem with an orbiting system however is that the individual elements have large relative velocities, the component of these velocities that is in the line of sight direction leads to mismatch in the arrival visibility phase of the incoming radiation over the course of a single integration. Of course this happens to a far lesser degree in any interferometry system with large baselines, the effect is however more pronounced given the large velocities involved. The difference in the phase of the visibilities over the duration of the integration causes destructive interference within a single measurement. We can quantify this destructive effect by the decoherence:

$$D = \frac{I_{measured}}{I_{real}} \quad (5)$$

The decoherence (D) is thus the ratio of how much of the true intensity is actually measured and the true intensity (with a 1 representing that no decoherence takes place, and the signal is therefore completely coherent, and 0 is complete destruction of the signal). Figure 2 shows the decoherence caused by integration time in a number of directions. We can see that even small integration times can lead to almost complete destruction of incoming radiation in certain directions. Figure 3 shows that the full angular and frequency dependency of this effect. Lower frequencies are of course less affected due to their longer wavelength. The angular dependency is due to the way the orbits of the orbiting elements are aligned, the normal and anti-normal direction of the (average) orbit have a far lower relative velocity and are thus less affected. The directions that have less decoherence can thus be studied using longer integration times, this can be used to select orbits that are normal to a specific area that can be studied more in depth.

This effect for the other directions can be countered somewhat by modifying the integration times for different scenario's [13]. This can be done in two ways: direction dependent integration and baseline dependent integration. Direction dependent integration would scale the integration time up when studying the fields that are normal to the orbital plane; these directions do not suffer from the same rapid decoherence that other directions have (see figure 3) but it would limit observations to those directions increasingly as the integration time is scaled up. Baseline dependent integration would scale the time depending on the relative velocities of the satellites, a shorter time when the velocity vectors have a large difference between them and longer when they are in alignment. But even these operations have limitations on the amount of integration

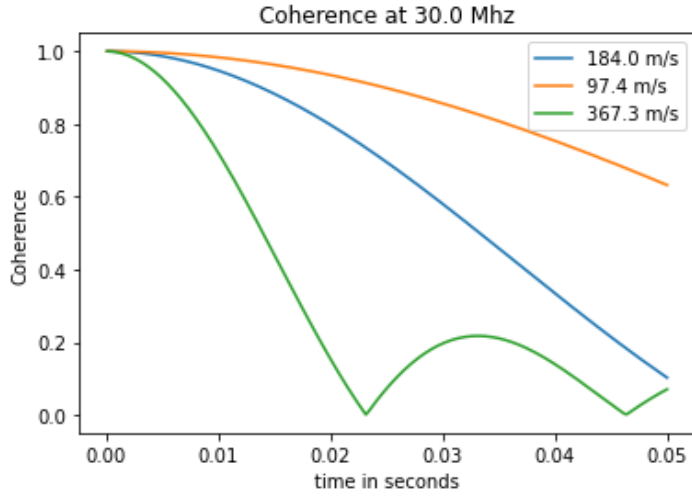


Figure 2: Decoherence in the 30MHz signal between two lunar orbiting radio antenna's. The velocity given is the difference in velocity between the two satellites along the line of sight to a hypothetical source.

time that is available for orbiting systems. Therefore these systems must have a (very) short integration time which in turn causes them to accumulate more data that has to be sent and processed than ground based systems.

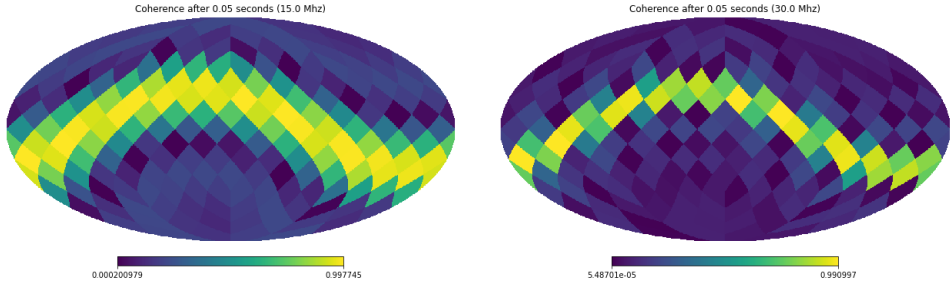


Figure 3: Decoherence has a strong angular and frequency dependency. Assuming the orbital parameters as proposed in section 5.

3.7 Synchronisation and localization

Interferometric measurements depend highly on knowing accurately the (relative) positions of the individual measuring elements. On the Earth's surface this presents very little difficulty since the elements generally do not move in relation to each other. However in orbit the relative velocity of the orbiting elements present issues.

It is therefore imperative that the position of each element be known to a high degree of accuracy.

Figures 4 and 5 shows the effects of errors in the position on a hypothetical point source. A random error in the x,y and z position is introduced on the the orbiting satellites with the total average combined error on position set to the Gaussian mean.

Each measurement assumes an integration time of 0.1 seconds and the errors are independent of one another. The measurement moments are taken from a random set of position combinations over a 1 year mission duration. The visibilities measured by the system is calculated from the true visibility (using the real positions of the satellites), but the reconstruction for the image and the intensity of the point source is done using the positions with error applied. The results are a decrease in measured intensity of the hypothetical point source which decreases with increasing error.

At the lower frequencies a Gaussian error of about 1 meter only has a slight effect on the reconstructed image, the degradation is mostly a flat line up till one meter (figure 5). But a higher error (or at higher frequencies) the effect of positional errors become increasingly problematic. If the error cannot be gotten to the order of about a meter it is likely that higher frequencies ($> 30MHz$) cannot be accurately measured.

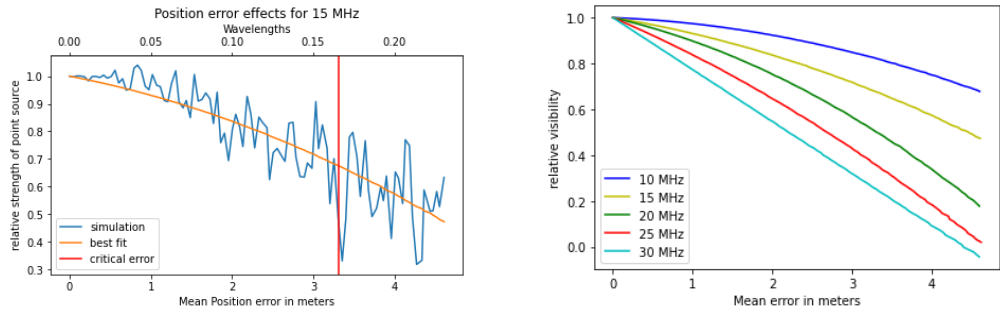


Figure 4: the effects of random Gaussian error in the position of each satellites (thus the total error is the compound of two errors) on the brightness of a point source. left panel shows the results from a simulation at 15 MHz, along with a trend line and the critical error amount where the point source brightness is overtaken by neighboring points. The right panel shows the trend line for different frequencies.

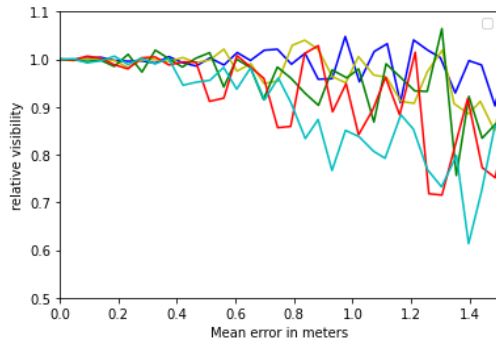


Figure 5: The effects of error. Same data as figure 4 but using the simulation data without trend line and zoomed in. The brightness remains constant for small errors (up to about 60cm).

4 Scientific objectives

The scientific data provided by a system capable of mapping the ultra-low frequency range of the electromagnetic spectrum is expected to be very bountiful. In this section a number of scientific cases are presented that can be performed with the system in mind. These science cases are used to distill some basic requirements for the system from this such as resolution, sensitivity, mission duration and data collection. Some of these will prove to be possible within the system and others will likely have requirements that cannot be performed within the proposed framework (but possible with an increase of the number of independent elements).

4.1 Ultra low frequency sky map

Very detailed radio sky maps have been made for many segments of the electromagnetic spectrum. Each of these maps have given us a greater understanding of the structures of the universe.

So far the atmosphere of the Earth has prevented us from making a similar map for the ultra-low frequency end of the spectrum. This has prevented the accurate identification of sources at these frequencies. But a system partially in orbit and on the surface of the Moon provides an opportunity to do exactly that.

Extrapolating from the 74 MHz Very low frequency sky survey (VLSS) the source count at low frequency can be approximated by [14][11]:

$$N_{>}(S) = 1800 \text{ deg}^{-2} \left(\frac{S}{10 \text{ mJy}} \right)^{-1.3} \left(\frac{\nu}{10 \text{ MHz}} \right)^{-0.7} \quad (6)$$

Where N is the number of sources per square degree of sky, S is the source brightness and ν is the frequency at which the instrument is looking.

Taking a conservative estimate of being able to distinguish sources of up to 100 milli-Jansky and at a frequency of approximately 10 MHz we should still expect on the order of a hundred visible sources per square degree. At a frequency of 2 MHz (below this frequency the galaxy starts to become opaque to radio waves) we can expect near to 300 sources per square degree.

Due to the presence of high levels of radio background it is difficult to distinguish faint radio sources at very large wavelengths from larger structures that are present. By doing longer observations the smaller sources can be distinguished.

We can express this confusion limit for the low frequency sources as:

$$S_{conf}(\theta, \nu) = 16 \text{ mJy} (\theta/1')^{1.54} (\nu/74 \text{ MHz})^{-0.7} \quad (7)$$

Where S_{conf} is the lower floor in mJy of distinguishable sources, θ is the resolution and ν is the frequency. Using the radius of the Moon as an approximation of the limiting factor on the resolution the confusion limit behaves as in figure 6.

$$t_{survey} = \frac{44d}{N^2} \left(\frac{s}{Jy} \right)^{-2} \left(\frac{T_{sys}}{10^7 K} \right)^2 \left(\frac{\Delta\nu}{100 kHz} \right)^{-1} \left(\frac{\nu}{MHz} \right)^4 \quad (8)$$

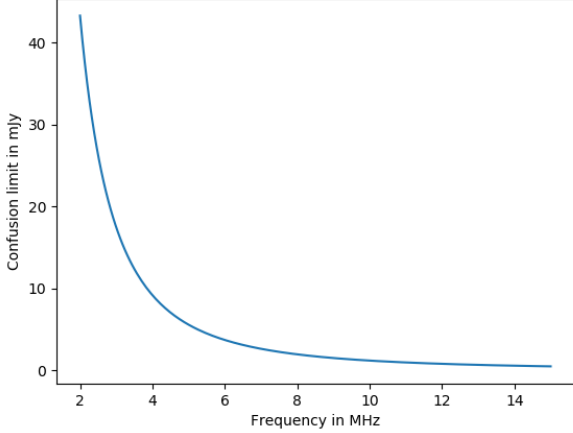


Figure 6: Confusion limit in mJy assuming a lunar radius baseline

Where t_{survey} is the time it takes to survey one steradian to $1-\sigma$ with point flux density to s. The amount of time estimated for confusion limiting is far greater than any reasonable time limit of the mission (order of 10.000 days to reach the confusion limit at 10MHz). However some of the brighter sources should be detectable as per equation 7. If we take some modest figures: 10 Janksy as a detection floor at 10 MHz. It would still be expected to find 1 source for every 5 square degrees or more than 20.000 sources over the full sky (although likely the system would only reliably survey half the sky).

4.2 Active Galactic Nuclei, feedback and fossil radio galaxies

4.2.1 Low frequency spectrum

Active galactic nuclei (AGN) deposit a lot of energy in their surrounding regions through their relativistic jets. These jets emit radio waves mostly through synchrotron radiation. This radiation has the property that the energy is dominated by the lower energy electrons, these lower energy electrons have much longer cooling times than their higher energy counterparts. This causes older jets to have a very steep energy distribution. Therefore lower frequency observation can probe the older jets in a way that is impossible at higher frequencies[15].

The radio lobes of AGN's are not typically affected by optical-depth effects. Since the normal synchrotron self absorption mostly occurs when the source is sufficiently compact as well as because the surface brightness temperature being well below the 10^{12}K for the inverse-Compton catastrophe. In hotspots however the catastrophe does occur. These two effects change the spectral shape from the optically thick $f_\nu \propto \nu^{-0.7}$ to $f_\nu \propto \nu^{\frac{5}{2}}$. This turnover occurs at the shock front of the lobes and the frequency where this occurs, which is typically well below 100 MHz, can be used to deduce features of the radio lobe such as magnetic field strength within the lobe [11].

The interaction of the AGN jets with their surrounding is not properly constrained as of yet because very little is known about the low frequency spectrum below 100 MHz. In addition this frequency is further shifted downward due to redshift for older objects. The jets of AGN tend to be very bright and even brighter at lower frequency. This in

addition to their angular size (The jets of Centaurus A stretch a few degrees from the host galaxy) which is also assumed to be even larger at the lower end of the spectrum, make these objects good targets to study with this interferometer setup. At least up to a few tens of millions of parsecs. Radio galaxies are relatively common when talking about such distances and present in a large range of sizes, the largest of which easily fall within even the most pessimistic angular resolution of the system. Therefore it should be possible to find at least a few that can be studied over the full spectrum of the system.

4.2.2 Dying and fossil radio galaxies

The active phase of a radio galaxy is believed to be a time when the central black hole is actively accreting matter. An unanswered question about this process however is how long these active phases last. So called "double-double" radio galaxies, where there are two distinct sets of radio lobes, are however very rare. This suggests that quickly successive phases of feeding are rare [11]. A better method to answer questions about these cycles can be to instead find "fossil" radio galaxies. These galaxies will have exited the feeding phases recently ($< 10^7$ years).

The cooling time for the electrons in the jets is however inversely proportional to the energy of the electron. This allows low frequency observation to detect the remnants of these jets at a far larger rate than previously possible.

Some efforts have been made to identify radio galaxies in the process of dying [16] [17]. These studies have however been limited to higher frequency observation and are therefore limited to small number statistics. The lower frequencies that are available at a lunar orbit would allow the detection of more of these galaxies, thus giving a better understanding of how often active phases occur in galaxies.

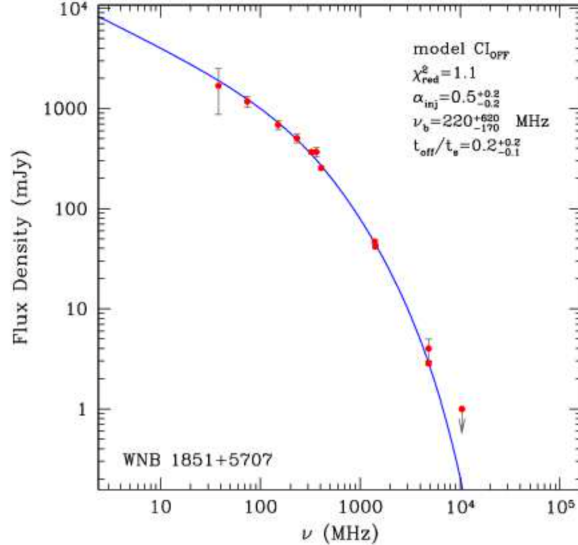


Figure 7: Measurements and fitted model of the spectrum of a radio galaxy believed to be in the process of dying out, from Murgia et al. [16], note the high brightness at low frequency

4.3 Cosmology

One of the most sought after tests for discriminating between cosmological evolution models for the early universe (the cosmic dark ages) is that of the global 21cm signal caused by the hydrogen flip at the very early universe, and therefore at very high redshift. This signal itself has not been measured yet (although missions are currently trying to do just that like NCLE). Therefore measuring this signal itself remains a scientific target for any low frequency mission. However with higher resolutions available to interferometric systems a second objective besides measuring the global signal presents itself: The anisotropy of the 21 cm signal. This anisotropy is expected to be embedded in the global 21cm signal. The signal is expected to yield constraints on cosmological models. The 21cm signal at very high redshifts ($z \geq 30$) can test the distribution of gas and clusters of mass in the very early universe. The test includes the measuring of the anisotropy at frequencies lower than 50MHz, where the smaller fluctuations at large ℓ ($\ell \geq 5000$, corresponding to an angular scale of ≤ 0.036 degrees) encodes the differences between differing cosmological models[18].

Though other missions have already attempted to probe the 21cm signal in space (NCLE is a good example) the measurement of the signal and those fluctuations at the higher order terms require a resolution that cannot be achieved with a single element (thus a single locations with a very short baseline) system. Therefore an interferometric system has the best chance to measure these terms.

Since at the higher end frequencies of the proposed investigation we can probe angular resolutions of approximately an arcminute the maximum ℓ that can be probed the maximum value for ℓ lies in the best cases at over 6000 (≤ 0.03 degrees). The limiting factor however is that these signals are generally weak, therefore it would require a significant reduction in noise to be able to differentiate signals coming from the cosmic dark ages. A large number of dipoles would be the solution in most cases, however a long time for measurements could achieve similar results. Taking the estimate from Jester et al.[11]:

$$T_{rms} = \frac{D_{max}^2 T_{sky}}{A_{eff} \sqrt{N(N-1)t_{exp} \Delta\nu}} \quad (9)$$

Where T_{rms} is the root mean square of the measurement error, D_{max} is the maximum baseline, T_{sky} is the sky temperature, A_{eff} is the effective aperture area, N is the number of dipoles, t_{exp} is the measurement time and $\Delta\nu$ is the bandwidth. We can plug in the numbers of our system and arrive at a measurement length of 900 years to reach the milliKelvin level for 30 Mhz (this would be needed to probe the anisotropy of the global signal with arcminute scale resolution). This is the sensitivity needed for the very high order terms to be derived. The main barrier for measuring the signal at these frequencies is the effective aperture area factor (A_{eff}) which is a small quantity when only talking about a small number of elements present in a large section of space. For the signal at redshifts below $z=30$ (45 Mhz and above) the signal can be measured to the milliKelvin level on the order of several 100's of days. These estimates make it clear that a full arcminute scale anisotropy measurement is likely out of reach for a system with a modest amount of measuring elements. The global signal and degree scale resolution in the anisotropy however can be achieved using a modest setup like discussed here. This would require the system to be able to perform measurements over a larger frequency scale.

4.4 Planetary and solar emission

There are several questions about astrophysical phenomena within our own solar system that low frequency observations can help answer. These mostly focus on emission from

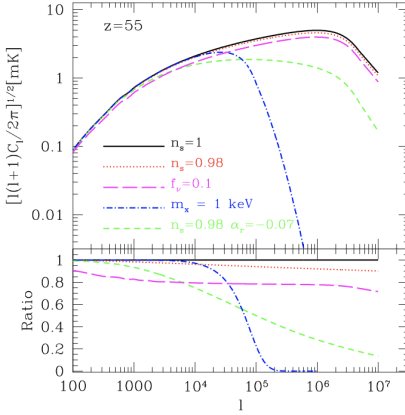


Figure 8: The effect of different models on the predicted anisotropy of the 21cm signal at $z=55$ (approximately 25Mhz). The top panel shows a number of different models and the bottom panel shows the relative fraction between the models. taken from Loeb et al.[19]

the sun and the two gas giant planets.

4.4.1 Coronal mass ejections

The sun itself emits powerful radio bursts in the form of coronal mass ejections (CME), these ejections of plasma from the solar surface lead to a phenomena called a magnetic storm. These emissions are of particular interest due to the harmful effects they can have on electronics and humans in space. As the CME propagates away from the sun the spectrum of the emission by the magnetic storm shift to be primarily composed of the lower frequency components. Therefore low frequency observations can trace the CME much further out into the solar system than possible from the Earth, although still not as far as the Earth's orbit. The frequency dependence is shown in figure 9 [20]

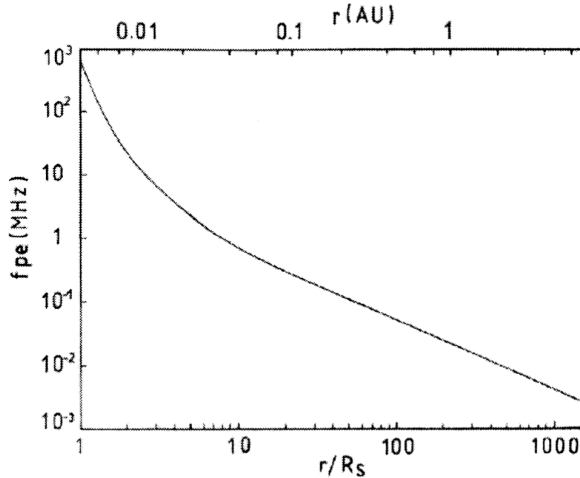


Figure 9: The peak frequency of CME emissions as function of the distance from the sun, image taken from Mann et al. [20]

These observations would allow for better modelling of the space weather phenomena and better understand the propagation of the hazards they entail.

These observations would require a cadence of measurements sufficient to track the propagation of the emission. Taking an average velocity of CME's from the sun (~ 1.000 km/s), the CME would dip below observable frequencies on the order of 30 minutes in which time many measurements would have to be taken to follow the propagation, therefore minute long integration times would be detrimental and unnecessary since these events are very bright.

4.4.2 Planetary emission

Strongly magnetic planets are a source of bursts in low frequency radio emissions. Especially Jupiter can have outbursts that are fueled by cyclotron maser instability and comparable in strength to that of the Sun [21]. One of the open questions about these discharges is the occurrence rates and duration of these flares. A wide statistical is needed to constrain these parameters. The emissions from these events is circularly polarized which allows them to be distinguished from the emissions from parent stars. For a system that is not sensitive to differences in polarization however the time dependant nature of the burst can be used for detection. the burst are typically on the order of 15 minutes however examples of burst lasting several hours have been detected [21].

Although the achievable resolution for the proposed system is likely to be insufficient to exactly determine the origin of the burst they do provide a starting point for further investigations.

Another interesting emission from Jupiter is the auroral emissions. these emissions are caused by the interaction with the solar wind and the magnetic field of the planet. These emissions are constant but do vary in strength over time, bursts in the case of Jupiter can last from a few hours to several days. The activity of the emission is dependant on the solar wind activity [22].

The distribution of these emissions gives insight into the magnetic field of the planet. Another reason to accurately measure these emissions is that they can be compared to emissions picked up from extrasolar Jupiter like planets. This is discussed further in section 4.5

The spectra of these emissions (see figure 10) lends itself well to low frequency observations. Many of the emissions would be undetectable by a Earth based antenna. Table 1 gives some of the system requirements to detect the planetary emissions [8].

A third interesting science case is the detection of lightning within the gas planets. The frequency and intensity of lightning has important ramifications on the chemistry present in the atmospheres. As well as a glimpse into the thick inner atmosphere of the gas giants. But details on the frequency, intensity and spatial variability of this lightning is scarce [23].

In a similar vein an interesting target of opportunity is the detection of lightning emission in the atmosphere of Venus. The question of whether lightning does exist on the Earth's sister planet is still an open one. The presence of lightning in the clouds of Venus has again huge ramifications for the chemistry allowed in the upper atmosphere [24]. Though since little is known about this emission this can only be considered a secondary target at best.

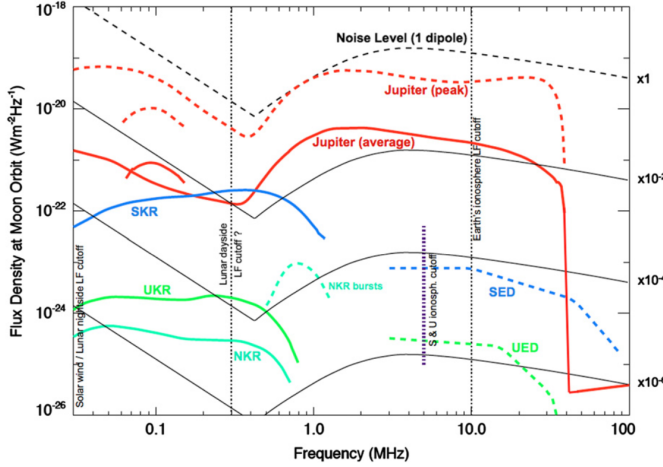


Figure 10: The spectra of several planetary emissions, Saturn Kilometric radiation (SKR), Uranus Kilometric radiation (UKR), Neptune Kilometric radiation (NKR), Saturn and Uranus electrostatic discharges (SED, UED). Jupiter electrostatic discharges follow the spectral shape of the SED and UED but lie above the image (between two to four orders of magnitude above). Image taken from Zarka et al. 2012. [8]

Radio Emission	b (kHz)	N (dipoles)	τ	$N(bt)^{1/2}$
Jovian radio emission	10	1	1 seconds	$10 - 10^2$
SKR	100	1	10 seconds	$10^2 - 10^3$
UKR, NKR	200 - 500	1	10 - 60 minutes	$10^4 - 10^5$
SED	10^4	10^2	300 ms	10^5
UED	10^4	10^3	300 ms	10^6
Radio exoplanet	$2 * 10^4$	~ 10	1 day	10^7

Table 1: Requirements to measure various planetary emissions [8]. b is the bandwidth, N the number of dipoles, τ is the integration time and $N(bt)^{1/2}$ is the combination of the elements required for $1 - \sigma$ detection. Assuming a 7m dipole. The electrostatic discharges (SED, UED and Jupiter discharges) last only on the order of 300 ms so a longer integration will make these discharges undetectable

4.5 Exoplanet and dwarf emissions

As noted in the previous section strongly magnetized planets (such as Jupiter) can emit radiation at frequencies below the atmospheric cut-off. This presents us with a novel approach for the detection of these planets in other star systems. Of course the emission from a Jupiter analogue will be too weak to be detected. But so called "hot Jupiters" that orbit closely to their parent star can emit radiation that is orders of magnitude stronger [22].

Similarly brown dwarf stars also exhibit emissions due to similar mechanics as gas giants. The same technique can be used to identify these stars.

These magnetized planets would emit bursts through the Cyclotron maser instability. This radiation is always fully circularly polarized which presents an easy method of distinguishing between emissions from the star (that is not polarized) and the planet. Grießmeier et al. [25] have identified four primary modes that trigger the emission. The two of most interest (because they are the strongest) are the emissions triggered by

CME's and the magnetic energy flux of the stellar wind.

The CME model relies on the energy input of a solar burst and are therefore not a continuous occurrence. CME burst duration is on the order of 15 minutes (although bursts of several hours are possible) which would require a large number of dipoles to detect in the time allowed, a 15 minute 10 mJy 3MHz burst at 25% bandwidth would require 10^4 dipoles. This requirements likely prevents the proposed system to detect these types of emissions. However a possibility still exists by looking at M class stars that tend to exhibit more violent eruptions at a far larger rate than other stars (tens of CME's per day).

The magnetic energy flux model however depends on the strength on the (continuous) solar wind and the magnetic field present between star and planet. This mode they found can easily be as strong as the CME emissions and in some cases even stronger. Figure 11 shows expected fluxes and peak frequencies of a number of known exoplanets in both the CME model and the magnetic model. In the magnetic model there are a few planets with reasonably high fluxes in the magnetic field model below the atmospheric cut-off.

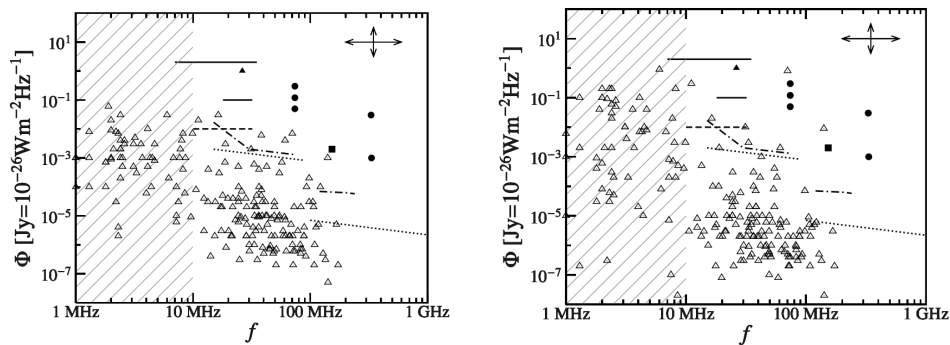


Figure 11: expected flux of the CME model (left) and the magnetic model (right). The open triangles are predictions for known exoplanets, solid lines and circles represent previous observation attempts

Several targets have been identified within the known exoplanets. Of those that have been modeled the best candidates for a positive detection are (taken from Grießmeier et al. [25]):

- HD 41004 B b, is the best case for the magnetic energy model with emissions below the atmospheric cut-off, the mass of this object indicates that it is a brown dwarf instead of a planet.
- Tau Boo b, which is the best case in the magnetic energy model with emission above the ionospheric cutoff, which can be used to combine measurements from ground and space.
- HD 189733 b, which is the best case in both the magnetic energy model and in the CME model below the cut-off and likely is a planet.
- HD 73256 b, which has emission above 100 mJy in the magnetic energy model and which is the second best planet in the kinetic energy model.

Especially the targets HD 41004 B b and HD 189733 b can be used as targets to try and confirm the magnetic energy model.

The only requirements this adds is to sensitivity of the measured flux. The expected flux of these targets ranges from several Jansky to hundreds of milliJansky. This would require a sensitivity that is at least of the same order of magnitude. This would likely require a large amount of antenna's to get to the confusion limit in any reasonable time frame for the lower end. A brighter "hot Jupiter" can be detected with a smaller total collecting area (see table 1). If only circular polarized light is considered however (meaning non circular gets filtered out) the time required would be reduced. It would require the system to be able to distinguish polarization for the weaker sources.

4.6 ISM probing

Low frequency observation can be used to infer details about the structure of the interstellar medium (ISM) in the solar neighborhood. As previously noted the galaxy becomes transparent to radio signals around 2 MHz. This frequency slightly depends on the angle of observation, observation into the galactic plane are foggy up to 2.5 MHz and going to lower frequency as the angle away from the galactic center increases. But below 2 MHz the distance one can see is determined by the structure of the local ISM and using reasonable assumptions is given by:

$$D(\tau = 1) \approx 100 \text{ pc} \left(\frac{n_e}{0.123 \text{ cm}^{-3}} \right)^{-2} \left(\frac{T_e}{7000 \text{ K}} \right)^{3/2} \left(\frac{\nu}{1 \text{ MHz}} \right)^2 \quad (10)$$

This allows one to cycle through the frequencies between 2 and about 0.3 MHz to see the galactic plane in absorption instead of emission against the emission of the warm interstellar medium. The visibility will then be set by the structure of the surrounding ISM. Peterson and Webber [7] have proposed a model for the transmission and emission within these frequency ranges that can then be matched with the observations to create a model of the ISM.

The requirements on the system for these observations are relatively modest. The scale of local bubbles are around a 100 pc up to an average distance of 1 kpc. This leads to a only degree scale-scale resolution. The sensitivity needed is also a modest one part in 1000 of the background level ($T_{RMS} \approx 10^4 \text{ K}$) [11]

4.7 Origin of cosmic rays

The origin of cosmic rays has been an area of scientific interest for some time. A lot of progress has been made over the preceding decades but many questions still remain. Especially the origin of cosmic rays has many theories that require confirmation. A radio interferometry system can answer some questions as to the origin of cosmic rays from within the Milky Way. As cosmic rays travel through the interstellar medium they emit synchrotron radiation. By observing known HII regions, which are optically opaque at frequencies below 30MHz we can be assured that any emission below this cutoff is emitted by processes in front of these regions. A correlation can then be done with gamma-ray astronomy to generate a (limited) map of cosmic ray arrival directions [10].

Though this would a very interesting study to perform the requirements on the performance of the system would likely be out of reach for the system as is proposed. To perform these observation a resolution requirement of the order of arcseconds is suggested to me necessary, although this is not entirely out of the realm of possibility for the higher end of the observations it is certainly not doable at 20MHz or below (see section 3). In addition the sensitivity would need to be on the order of milliJansky. This

can likely only be achieved by a much larger collection area than with a small number of dipoles on satellites.

4.8 Lunar Ionosphere probing

There is a lot of interest in the scientific community to establish a large radio array on the far side of the Moon. This project would require a better understanding of the Lunar ionosphere. The Apollo missions established that the plasma frequency (and therefore the cut-off frequency of observations) lies between 0.2 and 1 MHz on the day side of the Moon. This is expected to be lower on the dark side but no measurements have been done to determine this.

The distributed nature of the proposed setup, one station on the ground and two in orbit, allows for a direct comparison of signals between them. This allows at least a mapping in time of the behaviour of the ionosphere and how the plasma frequency changes over the course of a lunar day. In addition it allows for the investigation into the reflective properties of the lunar soil for radio waves. These experiments would allow for a better understanding of the needs of any future projects to establish a radio observatory on the Lunar surface.

5 Lunar orbit

In order to properly assess the capabilities of the proposed system a selection had to be made about the orbital parameters of the three element system (two orbiters and one lander). The choices for the main orbiter and the lander are of course set by the space agency (CNSA) and cannot be altered in any significant fashion, but this leaves one assumed choice available, that of the smaller satellite. In this section a choice of orbit will be selected that in turn will be used for the full simulations of the system in the upcoming sections.

5.1 Stable orbit

In order to do the science as described in section 4 the observation will have to take place over a time-frame of preferably several years. This presents a problem in the case of lunar orbits since most orbits around the moon are inherently unstable. An unstable orbit can be maintained with enough fuel on board however especially for smaller satellites this can quickly become prohibitively expensive, a 1900 km orbit for instance would need approximately 150 m/s of Δv to maintain per year.

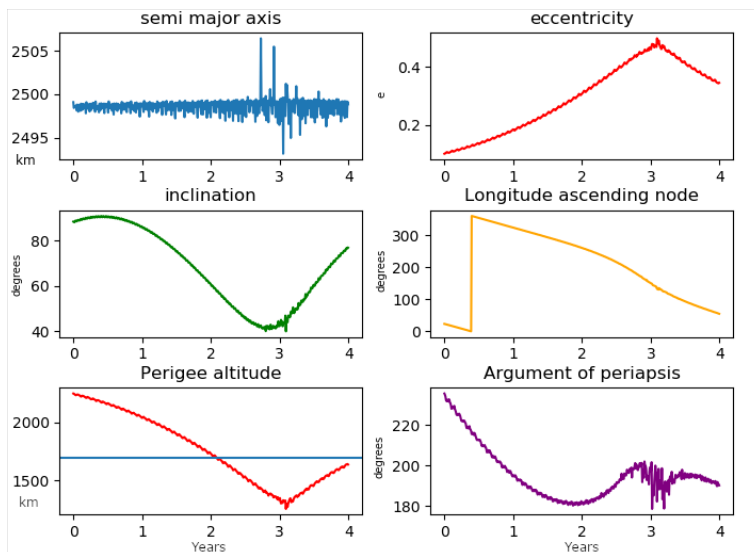


Figure 12: Kepler elements for a standard Lunar orbit over 4 years at 2500 km semi-major axis. The orbit eventually intersects with the Lunar surface (at 1700 km altitude), orbit was simulated with Tudat.[26] (Initial orbital parameters are measured with respect to the local Lunar frame in the case of the inclination, eccentricity and semi major axis and with respect to the Earth's vernal equinox with respect to ascending node, though placing the vernal point makes no difference with respect to the evolution of the orbit over long periods.)

Figure 12 shows the evolution of an arbitrarily chosen lunar orbit. If left without any stationkeeping the mission would end with a (rather spectacular) crash of the satellite into the lunar surface. in other cases the satellite would escape the moon entirely which is also a less than optimal situation.

Fortunately several "frozen orbits" have been identified. For these orbits the higher order gravitational effects cancel each other out. These orbits occur at inclinations of

27° , 50° , 76° and 86° degrees [27]. Further reduction on drift of the orbital elements in the moderate altitude range can be achieved by tuning the eccentricity around 0.04 and setting the argument of perigee to be either $\frac{\pi}{2}$ or $\frac{3\pi}{2}$ [28]. To confirm a full simulation of such an orbit was made for a 4 year duration in Tudat [26]. The results of the simulation are presented in figure 13. This simulation took into account the gravity field of the moon up to order and rank 30 plus perturbations from the Earth, Mars, Venus, Sun and Jupiter, along with radiation pressure (assuming an area of 1 m^2 and a radiation pressure coefficient of 1.2).

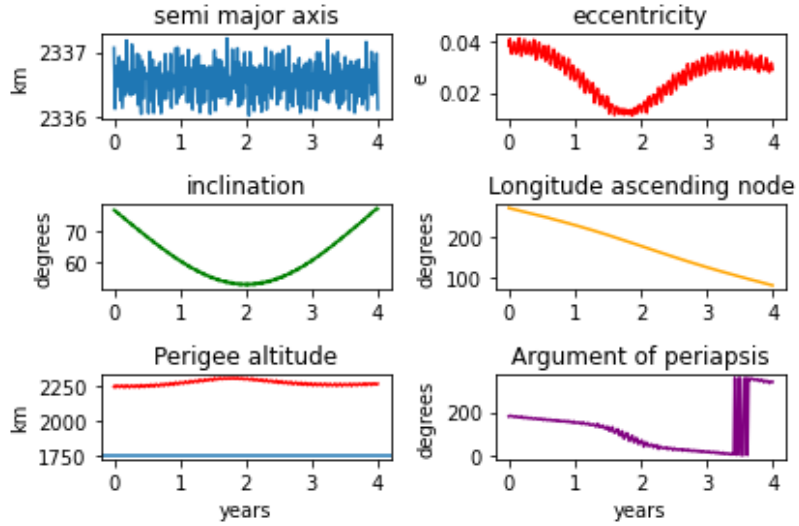


Figure 13: Kepler elements of a frozen Lunar orbit over 4 years with semi-major axis of 2338 km and a starting inclination of 76° degrees, there is some drift of the orbital elements over time but there is no escaping the moon or surface intersection.

As the figure shows the altitude of a spacecraft into this orbit will remain comfortably in lunar orbit for a long duration with minimal effects on the altitude and eccentricity. The inclination does change over the course of the mission as well as the longitude of the ascending node. Figure 14 shows the orbit at the start of the 4 year period and at the end. The precession demonstrated actually allows for a better coverage of the UV plane over the course of the mission since the orbit naturally twist around the moon in a predictable fashion.

5.2 Δv requirements

Since the choice of orbits that can be maintained over a long period of time is limited to these frozen orbits the only real choice left is which of these options is cheapest in terms of fuel to get into.

There are two basic options available for orbit selection, the extra satellite can "piggy-back" on the main orbiter and from its orbit change its orbital parameters to the desired ones, or a release of the satellite can be performed during the Lunar Transfer Orbit. In the first case the Δv for the lunar orbit insertion is provided by the main spacecraft but any inclination change would have to be done by the smaller satellite on its own. In the latter case any inclination can be chosen at the cost of a very minor amount of Δv (a few meters per second) but the orbital insertion burn would have to be performed by the satellite.

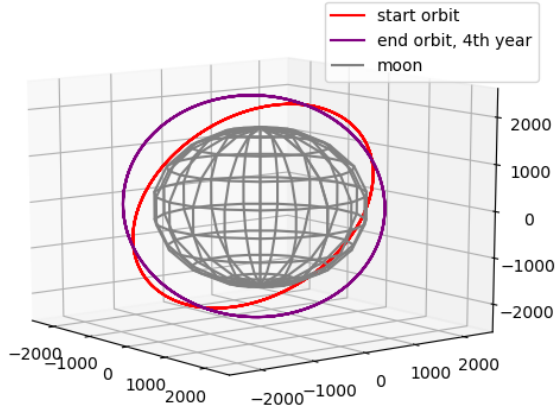


Figure 14: A representation of the same frozen starting orbit and after 4 years from a lunar-centric perspective.

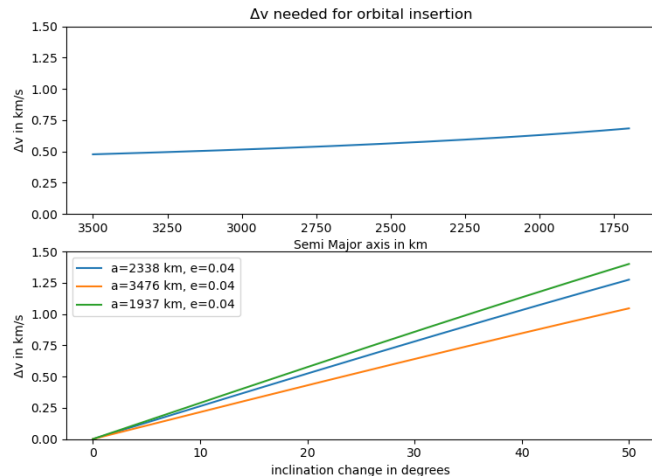


Figure 15: The Δv requirements for orbit insertion. The top panel shows the requirements for orbital insertion into an (almost circular, $e=0.04$) orbit with a semi-major axis as specified on the x-axis.

The second panel shows the Δv requirement for an inclination change at a number of orbits

Figure 15 shows the velocity change needed to either perform an injection burn (top panel) or an inclination change at a already established orbit (bottom panel). The velocity needed for an orbital insertion does not yet take into account any hyperbolic excess velocity introduced by the transfer orbit (this is therefore the Δv required for a perfect parabolic trajectory), this constitutes an absolute minimum rather than the full cost of an orbital insertion.

It is evident that the cheapest (in terms of Δv) is to make a small inclination change from the orbit of the primary satellite to the target orbit. Since the main orbiter would likely have to go into a near polar orbit in order to deliver the payload to the lunar pole we can assume that this orbit would be at or near the 86° stable orbit. The smaller satellite can change it's orbit to a 76° stable orbit for a cost of approximately 0.35 km/s of Δv .

For the purposes of simulating the system the orbits are therefore assumed to be as follows:

	a (in km)	I (degrees)	e	Argument of periapsis	Longitude of ascending node	True anomaly
Main orbiter / service module	2200	88	0.1	π	π	0
smaller satellite	2338	76	0.04	$\pi/2$	π	π
surface station	1737 (lunar radius)	-80, 10 latitude and longitude	N/A	N/A	N/A	N/A

Table 2: The initial starting orbital elements used for the simulations

6 Simulation setup

In this section the methods used for simulating the system will be explained. Since the proposal includes a system with orbiting elements, who are therefore moving with respect to one another, some different schemes than standard in radio astronomy have to be used.

6.1 sidestepping the w problem

Ordinarily the way to perform measurements in radio astronomy is to use the uvw plane (as in figure 16). However common practice is to correct for the w term, the vector pointing towards the source, and only use the u and v term and a delay term coming from the w term. This is usually fine for systems that are either small or have coplanar baselines, it can however usually not be done easily for larger systems or systems with a larger field of view. The condition that has to be satisfied in order to ignore the w term is as follows [6]:

$$(\sqrt{1 - l^2 - m^2} - 1)w \approx -0.5(l^2 + m^2)w \quad (11)$$

In the case of an orbiting system this condition cannot be guaranteed. The l and m terms are both the area of the full sky (and not limited to only a certain direction) and the w term is in most cases so large that any slight deviation in the other term will be magnified considerably. In addition any correction from time delay depends on high correlation in the time domain, given that the baselines for the proposed system are on the order of thousands of wavelengths this cannot be guaranteed either.

Other techniques do exist to deal with non-coplanar baselines, the most common of these is w-projection where the measurements made are then projected onto a field where the w term is exactly zero. These techniques are for example w-projection or w-stacking.

These techniques do however require knowledge of the extra path length between the antenna's, which in turn requires precise knowledge of the (relative) positions of the elements. Since the system proposed has two orbiting elements that have high relative velocities that would mean that for every individual measurement the baseline vector would need to be updated.

Since knowledge of the precise positions of the antenna's at every point in time is required either way a different technique was chosen for the simulations presented in this work.

The technique used essentially compares the measured phase for each antenna pair

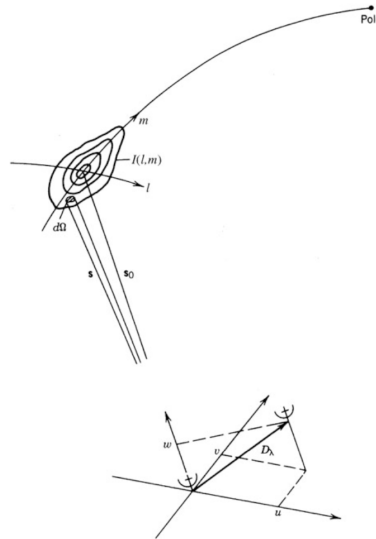


Figure 16: uvw plane

(baseline) to the expected phase that should be incoming from each direction on the target field (usually the entire sky). The technique is as follows:

1. The target field is divided into a selection of points (or hexagons).
2. For every baseline used in the sample the expected phase of each of the points is calculated.

$$phase_e = \text{angle} \left(\cos(2\pi \vec{D} \cdot \hat{x}) + i \sin(2\pi \vec{D} \cdot \hat{x}) \right) \quad (12)$$

Where $phase_e$ is the expected phase from the direction \hat{x} (the center of the hexagons) and D is the baseline measured in wavelengths. This is performed for every measurement (baseline) in the set and for each direction in the area of interest (usually the full sky). This creates a set of phases associated with each direction for every baseline. These phases are only valid for a single frequency (this must be done for every frequency separately since the expected phase will differ).

3. For each measurement the phases calculated in the previous step are now weighed according to the brightness in that direction (the pixel/hexagon associated with that specific direction) taken from the input model. These numbers are then combined creating a single (complex) number for every measurement. In this step there is an extra term that checks whether the Moon eclipses the line of sight for any of the two antenna's associated with that specific measurement, if this is the case the magnitude and phase coming from that direction is set to 0, and thus it does not add to the total number calculated for that specific measurement.
4. the phase coming from the input model (step 3), is compared to the expected phase of each point in the field and multiplied by the absolute magnitude of the measurement (the number made in step 3), as given in equation 13. This is done for every baseline in the set generating a separate field for every baseline. This creates a ring structure on the sky as presented in figure 17 top right.
5. Each of these field are then added together and each point is divided by the amount of times that direction was visible in the sample. See figure 17.

$$I_{total} = \frac{1}{n} \sum_{n=1}^n |I_n| * \cos(phase_n - phase_e) \quad (13)$$

Equation 13 shows the reconstruction of a single point on the field. I_{total} is the resulting intensity of the that particular point, n is the number of measurements that the specific point was visible (in effect not behind in the case of a wide field image), $|I_n|$ is the absolute magnitude of measurement n , $phase_n$ is the phase corresponding to measurement n and $phase_e$ is the expected phase from that direction given the baseline at measurement n .

This method allows the reconstruction of the intensity on the sky directly without having to go through deconvolution and fourier transformations. The downside is of course that the baselines and the phase distribution over the whole field will have to be known at every measurement. In this case that would not be such a large inconvenience because the same elements would have to be known in the case of w-projection as well.

In order to demonstrate and check the validity of this technique two test cases are first presented. These cases are easy to compare against the input model and against performance of a standard radio array.

The two cases are those of a wide field sky image and one of a single point source.

6.2 Sky map

The first case is that of a full sky image. On an empty field 8 randomly positioned sources are placed. The sky is in this case divided into 12288 pixels of equal size (this is a standard Healpix setting for an NSIDE of 2^5 , this is a modest resolution but this is just to show feasibility). And 2500 time point were randomly selected for the position of the satellites in lunar orbit and the ground station, these time points were selected from the from the 4 year Tudat simulation to simulate a full mission duration. In order to make the picture of a single measurement visible the baselines where shortened by a factor of 5000 to better display the progression of stacking baselines (if we took the full baseline the circles from the single baseline would not be visible in any plot), this because else the different phase positions would not be visible on a single image.

This setup does not yet take into account noise or eclipses caused by the Moon itself.

figure 17 shows the input model and the reconstruction of the measurements for a single frequency after a number of measurements (each measurement corresponds to three baselines since we have assumed three elements throughout this thesis) have been added together. It shows that already when a moderate number of baselines are added in this fashion the input image is faithfully reconstructed. The quality of the image improves further and further with increased amounts of baselines.

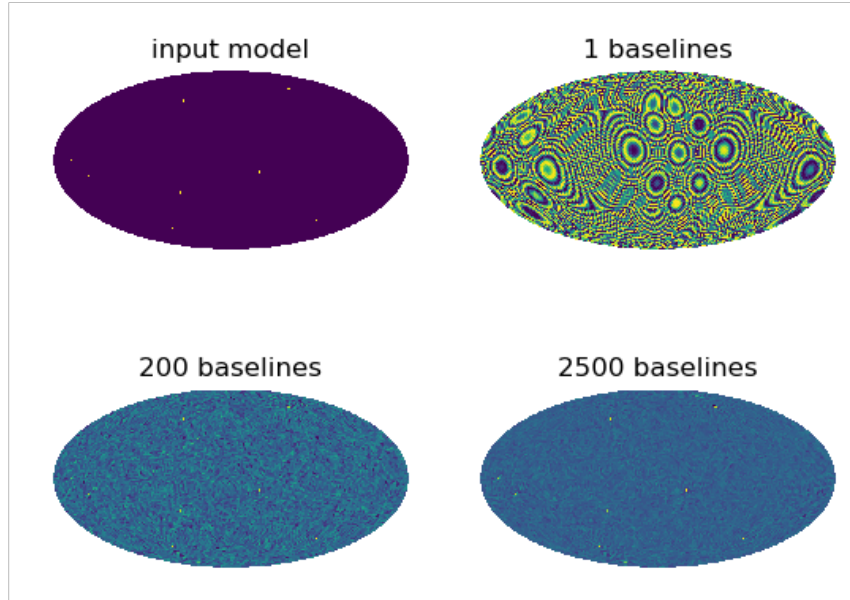


Figure 17: Mollweide view of the cumulative effects of stacking more measurements. Only a single pair of antenna's were used so in this case 2500 measurements is 2500 baselines.

6.3 single source PSF

The second test for the proposed method of creating an image is to look at the reconstruction of a single point source and whether it produces the same image as a normal reconstruction. In order to test this a single source was selected in a small patch of the sky. a thousand time-points were selected out of a possible two years of orbiting satellites, this corresponds to 3000 baselines (3 baselines for each time point). The orbits that are assumed for this test are taken from the tudat calculation for the single free choice element and the main orbiter is assumed to be in a station-kept near polar 88 degrees orbit. The surface station was selected to be at a latitude of -80 and longitude of 10.

The field of interest was made half a arcminute in each direction and divided into a grid of 300 by 300 directions. The phase center for this was selected in the direction that has the most average time visible for all three sub-elements.

From these baselines the uv coverage and the point spread function was calculated (figure 18). These results can now be compared to the test reconstruction of an image taken of a hypothetical point source with the same setup of the system (figure 19). To further investigate the performance of the system in a full sky image a number of other directions are also investigated. these directions are spread out over the entire sky. The results are presented in figure 20. The uv coverage is equally spread out for all observing directions except the direction that is directly in the radial direction of the surface and satellite orbit (directly away from the line between the surface station and the orbit). This direction would indeed suffer from a less complete uv sampling due to the way the orbit of the primary satellite and the location of the surface station lines up, however due the fact that the other satellite's orbit changes over time does mitigate the effect somewhat. The change in orbit is mostly driven by the inclination change (a maximum of 25 degrees, see section 5), this inclination change leads to a bigger sampling of the uv plane over a 4 year missions as shown in figure 21. This problem is unavoidable for certain direction but as shown is mitigated by letting the orbit of one of the satellites change naturally over time.

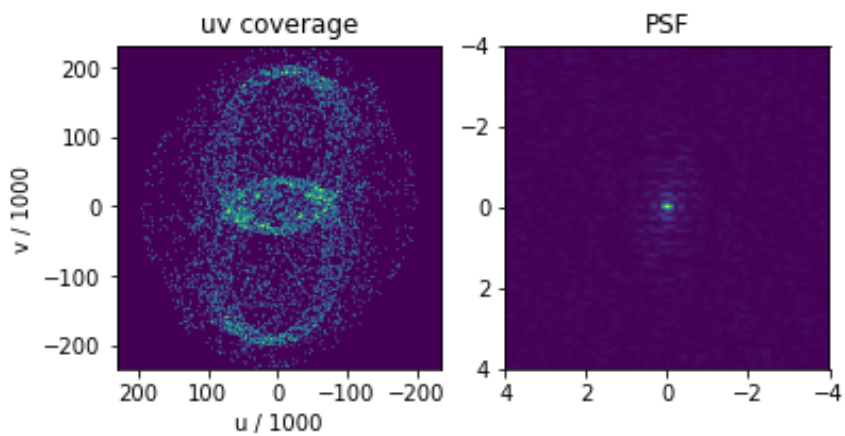


Figure 18: uv coverage of the selected baselines and the associated PSF in the direction of 140, 60 degrees latitude and longitude

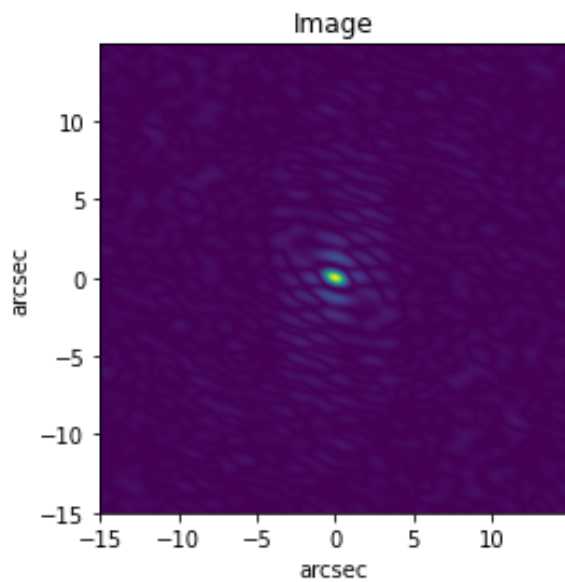


Figure 19: Reconstructed image of a point source with the same baselines as figure 18

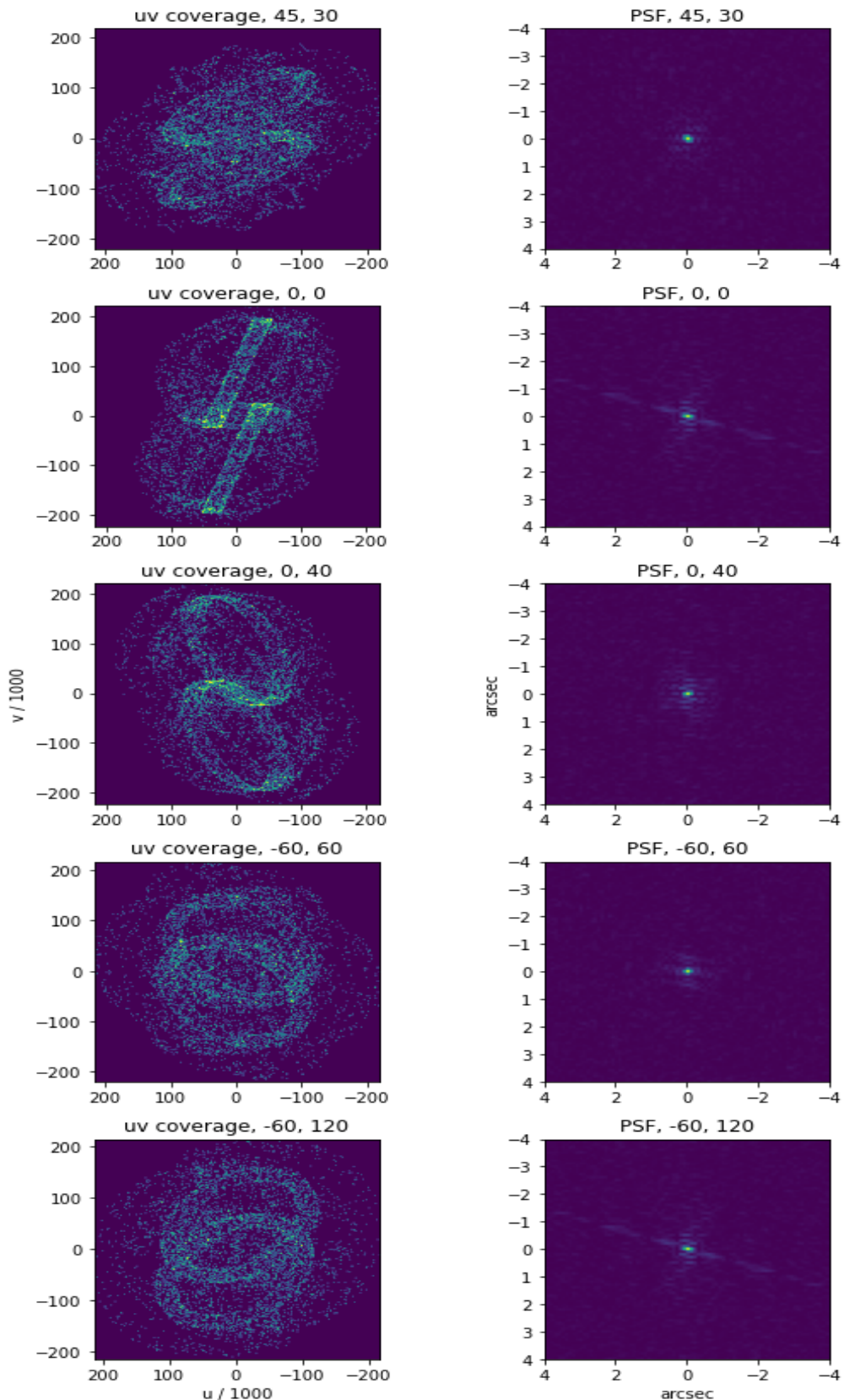


Figure 20: uv coverage and the PSF of the same baselines but in a selection of different directions, the directions are given in latitude and longitude. The second set of panels from the top shows the uv coverage in a radial direction from the surface station and satellite orbits.

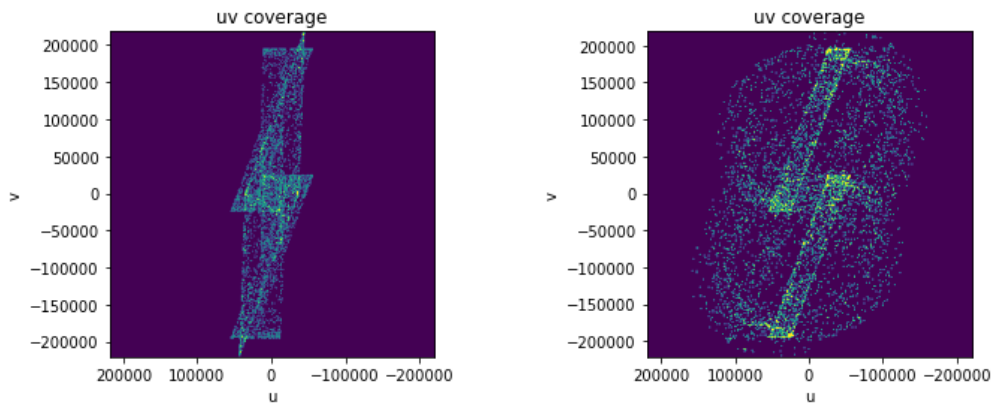


Figure 21: The left panel shows the uv coverage of a direction radial to the line between the surface station and an orbiting element if satellite orbit changes were not taken into account, the right panel shows it with these orbital changes taken into account.

7 Simulations

7.1 Setup

In order to test the viability of the system to achieve some of the science goals as stated previously in section 4 a single case was selected to perform detailed numerical simulations on. The verification of all science cases is outside the scope of this thesis therefore only a selection has been used in this case.

The science case that was selected is that of the fossil radio galaxies. These structures are expected to be fairly bright and cover a large section of the sky. Normal radio galaxies already cover sizes on the sky on the order of degrees, this should make them fairly easy to detect on a full sky image.

The simulations have been run at a variety of low frequencies, namely: 10, 15, 20, 30 and 50 MHz. These frequencies have been selected because 10 MHz is currently the lowest frequency that has sky map models available. 15, 20 and 30 have been selected because they provide an idea of the evolution that foreground emissions play at these low frequency observations and 50 MHz to provide some overlap with other already existing systems such as LOFAR.

To get a realistic idea of the performance of the system some factors have to be added to make it more true to the real environment in which the measurements would have to take place. The most prominent of these factors are the foreground emissions and the noise present in these low frequency measurements.

Another variable is the satellite dipole orientation. These have been chosen to be static with respect to the two orbiting elements (both point along the north south axis of the galaxy, thus having the highest sensitivity into the galactic plane), the surface element was taken to be normal to the surface and co-rotating with the lunar surface.

7.1.1 Input model

In order to get realistic simulation results an input model for the sky is required that simulates the foreground emissions present from the galaxy. Since the area of interest is the very-low-frequency range there are no accurate sky maps available. There are however a few models that go as low as 10MHz. The model used for the simulations comes from the pygdsim module, this contains a full sky model that ranges from 10MHz to 5THz [29].

Like previously stated, the objective of the simulation is to test whether we can accurately identify fossil radio galaxies at these frequencies, for this reason on top of the model a number of fictitious sources are superimposed. For the simulation three Gaussian sources are added relatively close to one another in the area that is most often visible given the lunar surface element (see next section) and outside of the bright galactic plane. Each of these sources has the same radius of 1 arcsecond. The three sources have a base intensity at 75, 150 and 300 Jansky at a frequency of 10MHz, the intensity falls off at higher frequencies using equation 14 (taken from figure 7).

$$I = I_0 * \left(\frac{\nu}{10MHz} \right)^{-0.5} \quad (14)$$

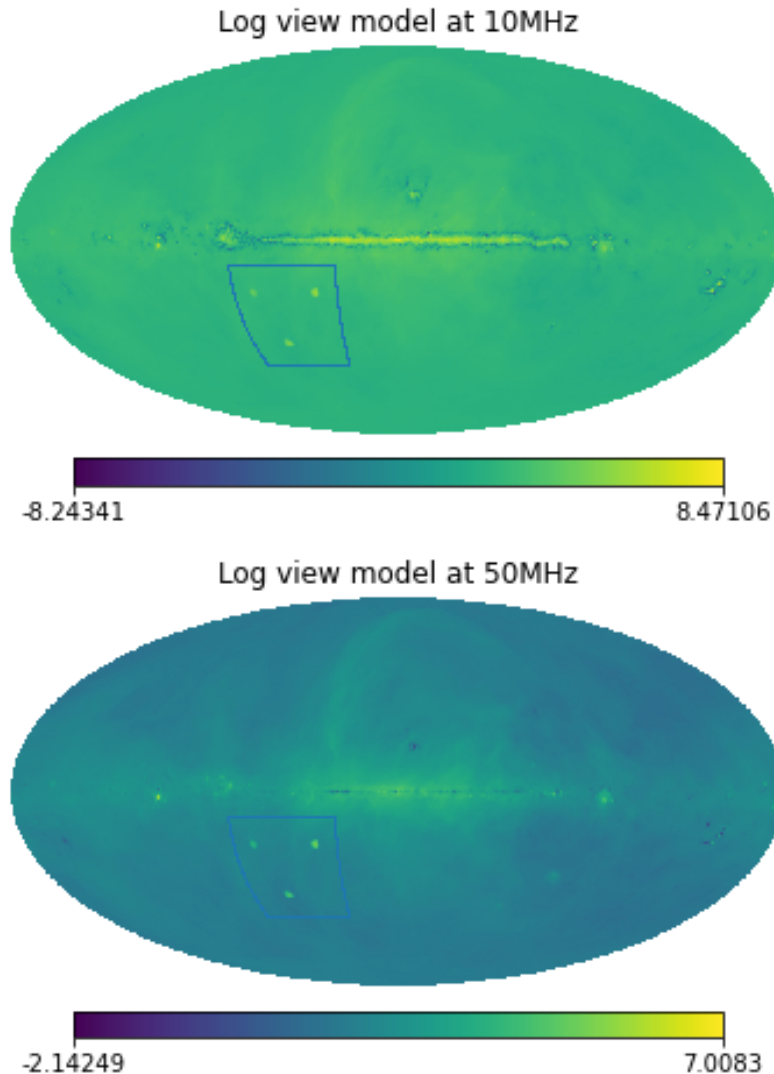


Figure 22: Input models for 10 and 50 MHz, in the highlighted field three sources are added. Units are in Jansky

Figure 11 shows two of the input models used. One at a frequency of 10MHz and one at 50MHz. A number of other maps have also been used (15,20,25 and 30MHz) but these two show best what the effects of higher frequencies are. The foreground emissions go down at ever increasing frequencies by a significant amount.

These model were used in a healpix map to project it onto the celestial sphere [30]. The projections used for the model were used in both a higher and a lower resolution, corresponding to a different number of pixels and therefore unique directions that were measured. The characteristics of the two maps used are given in table 3.

The very high resolution map is closest to what the maximum performance of the system could be considering the limits of the angular resolution would be (an arcmin at 10MHz, see section3). But this proved for the moment to be prohibitively intensive in terms of computing power needed to perform the simulations in a reasonable time frame

Resolution	NSIDE	NPIX	Angular size per pixel in arcmin
low	128	196608	27.5
high	256	786432	13.7
very high	512	3145728	6.9

Table 3: The characteristics of the healpix maps used (NSIDE is the primary healpix parameter for the map resolution)

(though certainly not impossible, especially with some tweaking of the code to make it more efficient). Therefore the simulations were performed with the low resolution and high resolution maps. Since even the low resolution leads to arcminute scales and fossil radio galaxies are expected to be on the order of degrees this resolution is sufficient to be able to give an indication on the performance (and therefore requirements) of the system.

7.1.2 Noise

The dominant foreground emissions are synchrotron emissions from electrons moving in the galactic magnetic field. The structure of these fields are not well known but they do lead to a very high surface brightness temperature in all directions (there is slightly less in the direction of the galactic poles but here we assume the worst case distribution as found in the direction of the galactic center). The main effect of these synchrotron emissions is that they dominate the system temperature and therefore limit any observations made for finding individual sources within the larger structure. It is therefore that for the purposes of investigating sources that these emissions can be categorized as noise. The noise is split into components coming from the (dominant) sky temperature and noise coming from the system.

For the sky noise a function was added that adds a noise factor to each measurement. The noise generated is given by equation 15 [11] [6].

$$T_{sky} = 16.3 \left(\frac{\nu_{MHz}}{2} \right)^{-2.53} \quad (15)$$

$$Noise_{rms} = 1.38 * 10^3 \sqrt{2} \frac{(T_{sky} * 10^6)}{(A_n * \sqrt{t_{int} * b})}$$

Where T_{sky} is the sky temperature in millions of kelvin, ν_{MHz} is the frequency at which the observation takes place in MHz, $Noise_{rms}$ is the root-mean-square of the noise factor in Jansky, A_n is the length of the antenna in meters, t_{int} is the integration time in seconds of each individual measurement and b is the bandwidth in Hertz. The value of the sky temperature for these frequency ranges is taken from Jester et al [11]. The simulation adds onto each measurement a gaussian noise factor (both in the real and imaginary domain) with the same RMS as the noise factor. To illustrate the effect of the sky noise at these low frequencies some numbers are given in table 4

At the low frequencies we are interested in the sky noise is going to be the most dominant contribution to any noise factors. In Jester it is even suggested that the sky noise is the only contribution worth considering since it is so dominant in this domain. However to preserve maybe a little more realism and for safety for the purposes of the simulation at the suggestion of Smith et al. [31] which argues that the noise added by

frequency in MHz	t_{int} in seconds	bandwidth in Hertz	$Noise_{rms}$ in Jansky
10	1	$1 * 10^6$	21689
10	0.1	$100 * 10^3$	216894
20	0.1	$100 * 10^3$	37553
50	0.1	$100 * 10^3$	3697

Table 4: $Noise_{rms}$ as a function of different frequencies, integration times and bandwidth

the receiver can easily be gotten below 0.1 times that of the noise from the sky using LNA matching. For this reason in the simulations the noise contribution from the sky was effectively multiplied by a factor of 1.1 to take into account the noise from the receiving system.

One of the key inputs in the amount of noise as presented in equation 15 is the integration time. In Earth-based systems there is a large freedom in selecting this parameter. As explained in section 3 the integration time for orbiting systems is fairly limited. figure 3 provides an estimation of the time-frame in which decoherence occurs. From this figure it clearly shows that integration times have to be very short, this however makes both the data rate required on the system prohibitively large and for the purpose of the simulation would make the simulations take very long. Therefore, in order to reduce the time for the simulations, it is assumed that techniques can be used that combat the decoherence effects of the orbiting satellites. Vertegaal et al. [13] have developed techniques that reduce this effect and claim that an integration time of 0.1 seconds is achievable for a system of Earth orbiting satellites, since orbital velocities for a lunar orbit are much slower than this an integration time of 0.1 seconds was considered as a safe assumption to be doable for the purposes of the simulation.

7.1.3 Orbit selection and surface station effects

The orbits used for the simulations are selected with a starting configuration that is compatible with the frozen orbits discussed in section 5. The parameters are described in table 5.

The time points used in the simulation are randomly selected from a starting lunar orbit with the following parameters, in order to speed up the code the simulations do not take into account the changes in orbit as was simulated in section 5 and instead uses orbits where the orbital parameters do not change over time (except the true anomaly). This changes what sections of the sky can be reliably monitored over the duration of the simulated mission depending on the selection of the initial parameters.

	a in km	i in degrees	e
Satellite 1	2200	86	0.1
Satellite 2	2338	76	0.04

Table 5: Orbital parameters of the two satellites, parameters are given in a lunar centric system.

The element of the system that is on the lunar surface is not one that can be controlled and therefore there are two general cases possible.

The first case is that the mission would indeed land on the lunar south pole and the

second one is on the far side on the moon, presumably somewhere close to the lunar equator.

The effect of this on the possible sky coverage for the system is given in figure 23. in either case it is clear that the best visibility is present to the normal and anti-normal direction of the orbits. The lunar south pole however does present an area with almost constant visibility (barring eclipsing from the Earth and Sun), this allows a certain section of sky to be investigated almost constantly which would certainly be useful for a number of the science objectives. Therefore the simulation has assumed the case of a lunar surface element present at a latitude of -80 degrees. This surface element is thus placed at what is effectively a semi-major axis of 1737 km which is connected to the rotation of the moon (and thus always stays at this latitude).

Since we have assumed dipole antennas the orientation of the antennas of each element has a significant effect on the measured radiation. Therefore a dipole function has also been added that takes into account the orientations of the different elements: $A_t = \sqrt{A_1 A_2}$. Where A_t is the total radiation measured, and A_1/A_2 are the directional dependent measurements for each of the individual antenna's (each use a Hertzian dipole function for direction dependent measuring). The orientation of the antenna's has been set to be aligned with the galactic equator so that their maximum receiving power is in that direction (effectively meaning the antennas are pointing towards the galactic poles). In addition for the purposes of the simulations the orientation of these dipoles is assumed to be unchanged. This means that the function that corrects for differing orientations in the simulation is not taken into account (and was disabled). The antenna of the surface element is set as normal to the surface (thus pointing up in the local frame) which co-rotates with the lunar surface. Since in this case the surface element is located near the pole it is pretty much all the time anti-aligned with the satellite elements. therefore the effects of changes of orientations are very small and did not play a major role in the simulations performed.

7.2 Results

The simulations are done to answer the question of basic system requirements. The question regarding requirements that these simulations are primarily supposed to answer is those of noise (or foreground emissions) in the system. Does the effect of using many baselines reduce the noise in a way that is expected and sufficient to identify the sources of interest (fossil radio galaxies) in a full sky map?(see equation 6 and section 4).

These are of course just two of the science cases proposed but these are the most easily checked for validity. The simulations were performed with a selection of different measurements and for varying frequencies. These measurements are taken from a statistical sample from a 4 year mission.

It should be noted that each measurement as described here actually corresponds to three baselines (three independent elements) and can be more accurately described as a set of baselines instead.

For the analysis, we take the results of these increasing number of measurements and assume that the pattern for increasing the amount of measurements holds for ever increasing amounts of measurements. This gives a general idea of the performance that a system such as this can achieve over a 4 year mission duration.

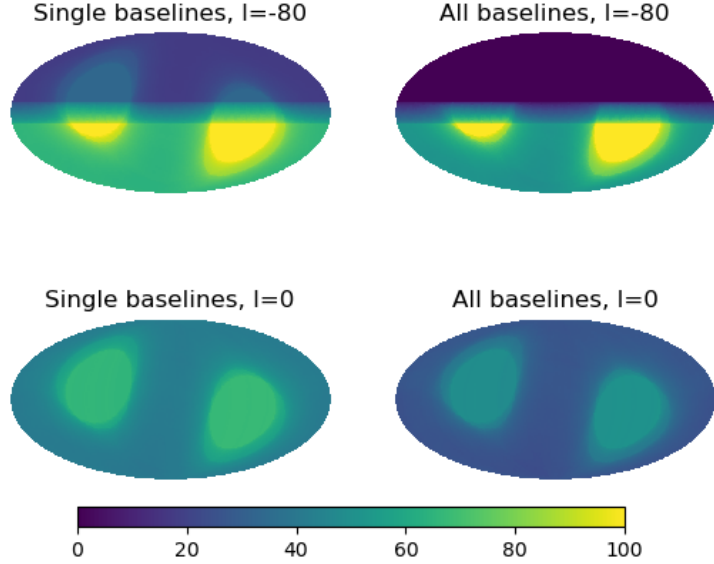


Figure 23: The effect of surface station location on the visibility on the sky. The image shows the percentage of time that each direction is visible, the left side shows the time that at least one baseline has visibility at a latitude of -80 (top) and 0 (bottom) degrees. The right image shows the percentage of time that all baselines have uninterrupted line of sight in that direction.

We will begin by presenting some of the simulations that establish the possibility of observing the large fossil radio galaxies that have been manually added to the input model. Then a more detailed analysis of the noise evolution is presented to establish how many sources a full sky survey should be able to identify.

The final section will describe the effects of a relatively simple CLEAN algorithm to further boost the visibility of low power sources at small measurement amounts.

7.2.1 Full sky image

An initial sense of the performance of the system can be made easily by a simple visual inspection. figure 24 shows the reconstructed maps at 10MHz, the frequency where the highest amounts of noise is present (see 6.1), from a 100.000 and 500.000 baselines (measurement times). It is clear by just looking at the coordinates where the manually added sources are supposed to be present that there is significant improvement between the two maps. The zoomed in view of the larger map shows that the noise reduces enough even at these moderate amounts to something that can easily identify the second weakest of the sources.

As previously discussed the amount of noise is highly dependant on the frequency. therefore figure 25 shows the exact same reconstruction only this time done at 20MHz. It already shows a significant reduction of the average noise present even in the smaller

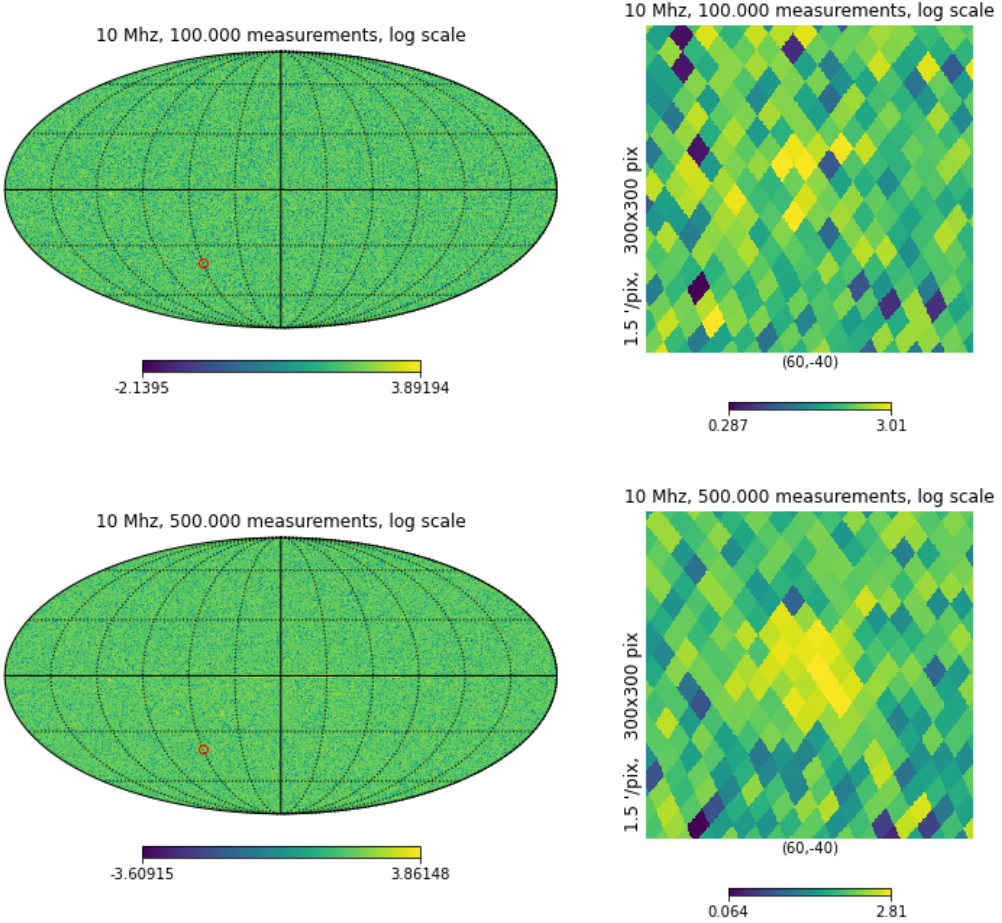


Figure 24: Two full sky reconstructions both at 10MHz, the top image is reconstructed from 100.000 measurements and the bottom from 500.000 measurements. The zoomed in gnomview for both images are of the same area. This is the location of the manually added medium strength source in the model 7.1.1, already apparent is that in the case of 100.000 measurements the source is not clearly identifiable, when 500.000 measurements are used the source becomes immediately visible. The scale of the images are in \log_{10} Jansky

amount of baselines (going from 10^3 to $10^{2.5}$ see figure 25 and 26) but also the weakest of the three manually added sources is already visible by mere visual inspection. For every tested frequency (10,15,20,25,30 and 50 MHz) this relation holds true. At higher frequencies the noise is reduced significantly (due to there being less noise present, see equation 15), and with a higher amount of baselines the added sources become more pronounced as well as some structure of the model becomes visible. This is best exemplified by going to very high frequencies as figure 26 illustrates. The even higher frequency and baseline count shows that besides the manually added sources some structure in the full sky starts to appear. The structure is not evenly distributed, specifically the upper half of the galactic structure lacks any form as displayed in the input model, this is consistent with the fact that due to surface element location certain area's are going to be under sampled.

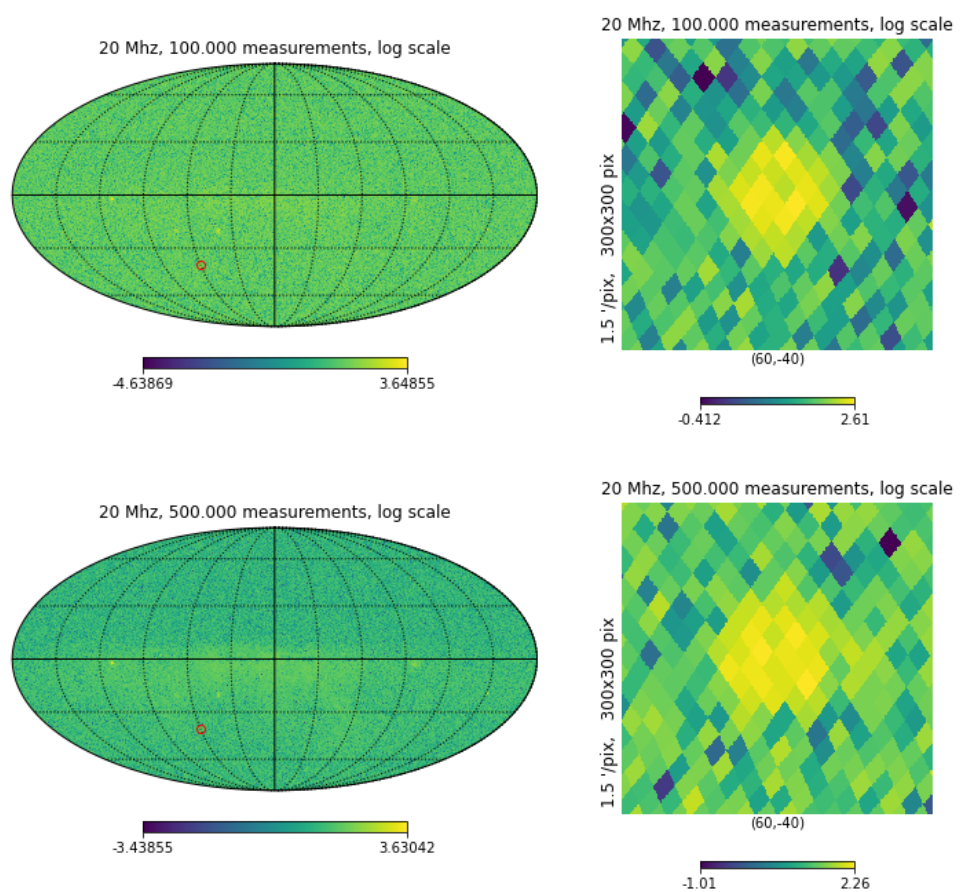


Figure 25: Same as figure 24 but now at 20MHz

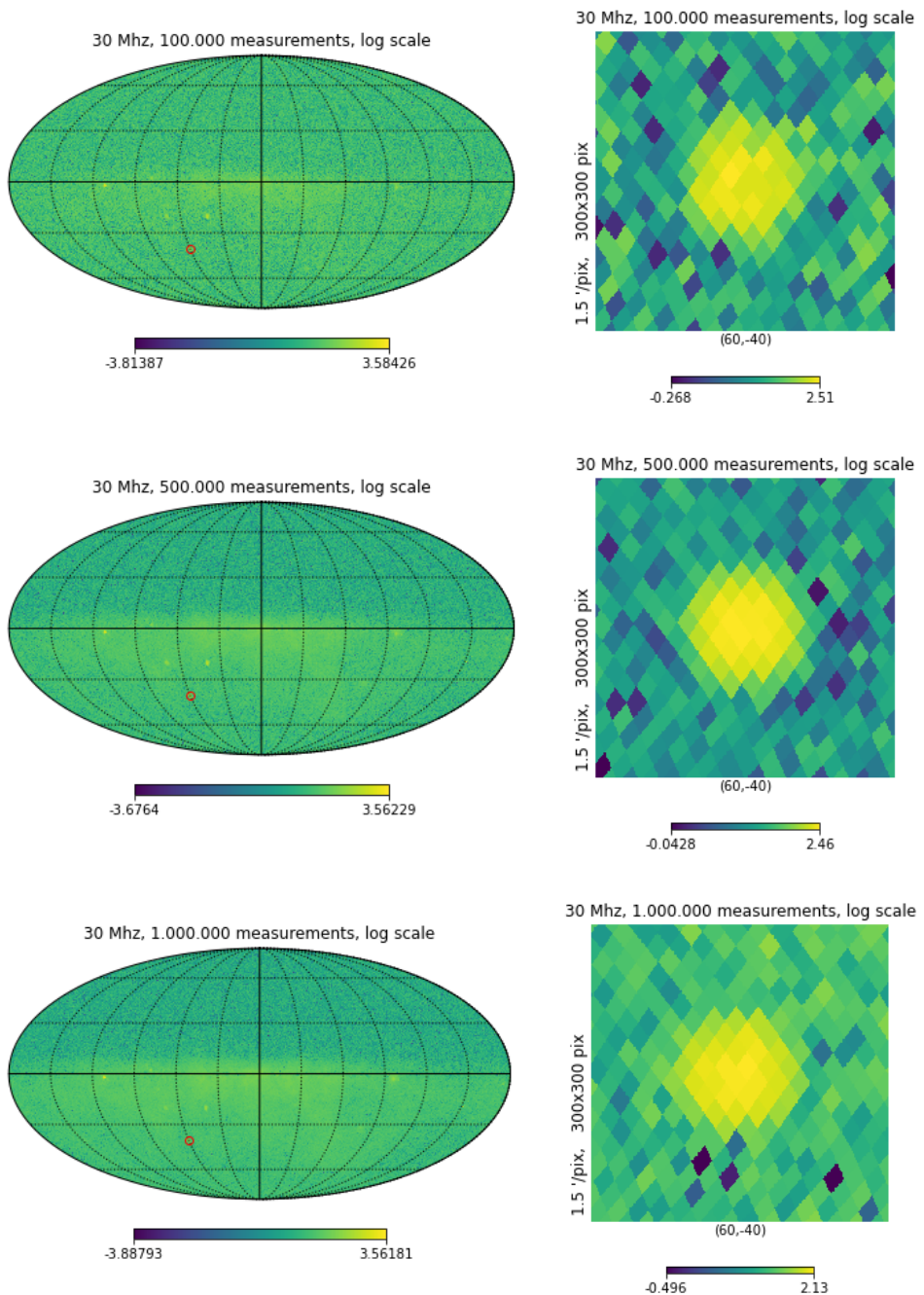


Figure 26: Top two panels are the same figure as before but now for 30MHz, the bottom panel is a reconstruction made with 1.000.000 measurements however to limit computer time this was done at a lower resolution than the other figures.

The simulations show that at least for large, relatively bright sources the system is more than capable of distinguishing these sources from the background/foreground.

7.2.2 Noise analysis

In order to make reasonable predictions about the amount of noise that would be present after the full mission the amount of noise must be first isolated. This is done by taking the reconstructions generated in the simulations and subtracting the input map from them. The map is then smoothed by reducing the resolution. Each new pixel now represents 110 square arcminutes instead of 13. This map of averaged residuals is illustrated in figure 27 for 20MHz. Already one feature of this map stands out and that is that the residuals in the top section is pretty much equal to the input map. This is again caused by undersampling of this area due to the placement of the surface element. Another feature that stands out is large residuals present where there are bright sources present. This is likely due to these spots being present just on the edge of the area that is always visible to at least one baseline and therefore also at least somewhat undersampled. To eliminate the effects of undersampling the top half of the image was completely ignored (figure 28). In addition to the masked pixels, the pixels with the highest values are also ignored to eliminate outliers (caused by bright sources and fringe effects such as poles).

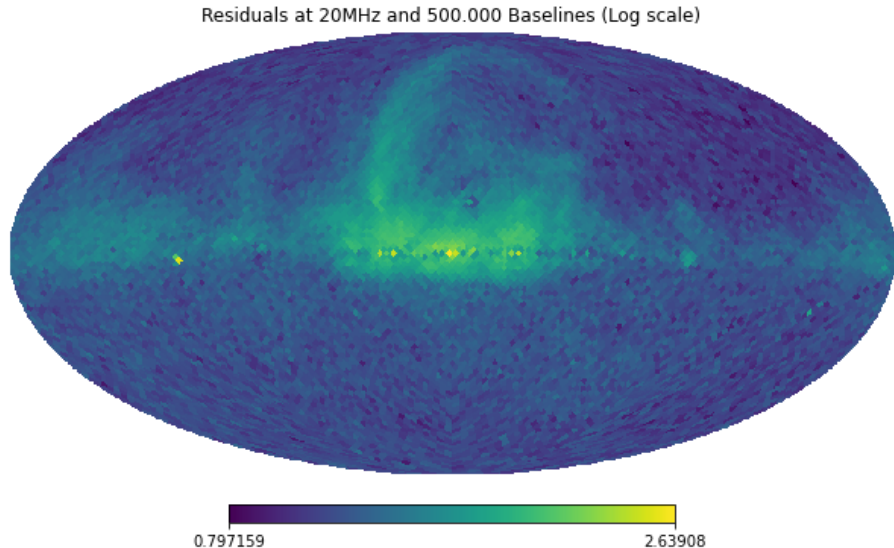


Figure 27: The residuals after the model was subtracted from the full reconstruction and each pixel was averaged over a set of 16 pixels in the original image

The average values of these pixels are presented in figure 29, the values are presented along with the theoretical predictions of noise reduction given larger amounts of baselines. The reductions in average noise power follows the theoretical predictions closely (the low frequency over-performs and the higher frequencies slightly under-performs the theoretical predictions).

The values presented in figure 29 can be extrapolated to longer timescales and more measurements. Since they follow the theoretical prediction pretty well it is assumed that this trend continues for a 4 year mission. Allowing for some downtime it is assumed that the total amount of measurements taken over a 4 year mission is about 1 billion (with a cadence of 10 measurements per second). This would mean the average noise would go down by a factor of $\sqrt{10.000} = 100$ compared to the 100.000 measurements as a starting value.

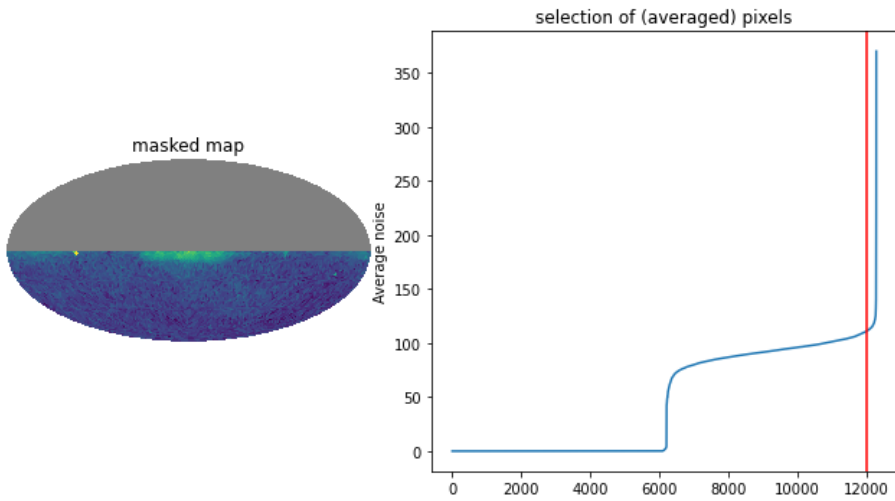


Figure 28: the left figure shows the masked map, all grey pixels are set equal to zero. the right figure shows the cut-off where pixels above a certain noise value are ignored, zeros (masked pixels) are also ignored in further analysis

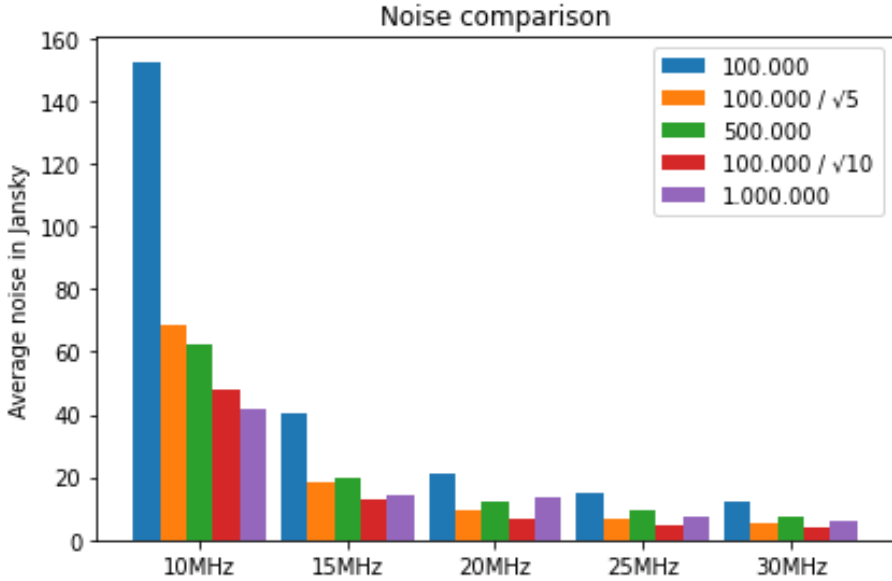


Figure 29: The average noise present in the selected pixels of the map, the numbers in the legend represent the number of measurements taken or the number of measurements taken divided by the theoretical degree of noise reduction.

The values found are then compared to equation 6 to get a prediction of the amount of new sources that can be discovered at these frequencies. figure 30 shows the lower limit in intensity of sources that can be discovered after 4 years and how many of these sources are predicted to be present per square degree of sky. Assuming isotropic distribution of these sources the resolution of the sky image (less than arcminute-scale at 30MHz) should be sufficient to distinguish the sources individually (see fig 1).

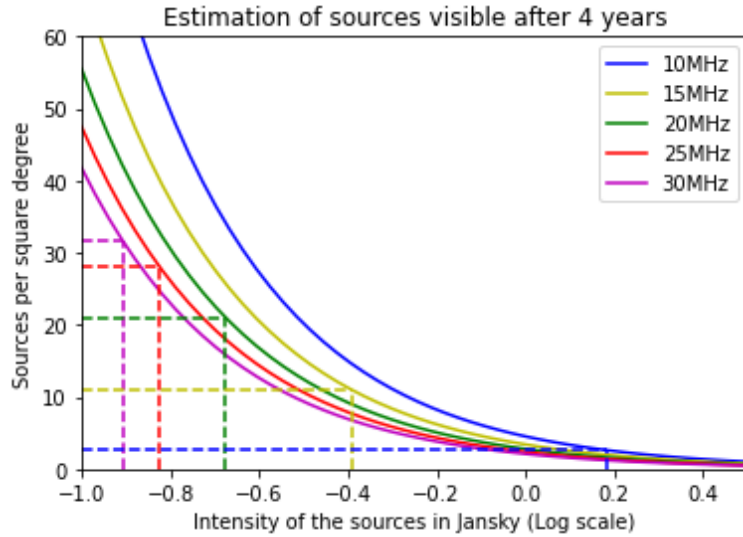


Figure 30: The number of distinct sources that are above a S/N ratio of 1 after the assumed measurements over a period of 4 years

7.2.3 Angular noise spectrum

Another way to characterize the noise present in the system is by performing an angular spectral analysis. The angular spectrum decomposes the sky image into a series of spherical harmonics. The value assigned to each harmonic is a measure of the total power contained in each mode (each mode is characterised by the wavenumber ℓ) of the deconstruction. It captures the (average) difference between points on the sphere, with higher modes containing information on the smaller scale, the zero mode for example captures the difference between the whole map for instance and higher order modes capture the energy present for smaller scales. To illustrate how a sky image is deconstructed into an angular power spectrum a number of dummy maps where deconstructed into these spectra and are presented in figure 31.

The primary use of these power spectra is to identify overall structure in a large field that cannot necessarily be identified by normal inspection. In particular small variations can be used to identify anisotropy (for example the small fluctuations in the CMB signal). The most important element that needs to be distilled from the angular power spectrum is whether any interesting elements rise above the noise present.

Therefore the noise residual maps (with the same selection and masking of pixels as in figure 28) were deconstructed into its angular components to get a sense of the evolution of the noise as the amount of measurements increase. The results for multiple frequencies are given in figure 32 and 33

Figure 32 shows that the angular noise decreases, as expected, with increasing frequency. It also shows that the decrease in noise closely follows the theoretical predictions for the reduction in noise. For lower orders of ℓ and higher frequencies we see that more measurements does not impact the noise present. This is likely due to the effects as previously discussed that the bright sources are not properly calibrated plus the fact that bright large sources are likely already better captured by even a modest amount of baselines. Therefore what we see is actually the structure of the galactic emissions present at lower orders of ℓ .

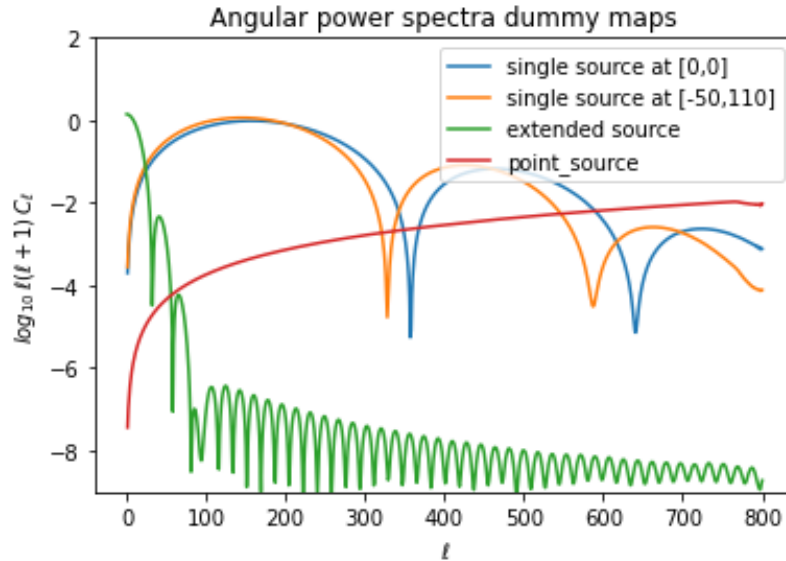


Figure 31: A number of empty sky maps are deconstructed into their angular spectra. ℓ is the mode number and $\ell(\ell + 1)C_\ell$ is the total power present in that mode. The single sources are 2 square degrees each, their angular power spectra show up in different modes because of different location (the one in the bottom of the field of view is for example not counted in the modes that check differences between top and bottom) but have equal integrated power. The extended source is 10 square degrees located in the center of field of view.

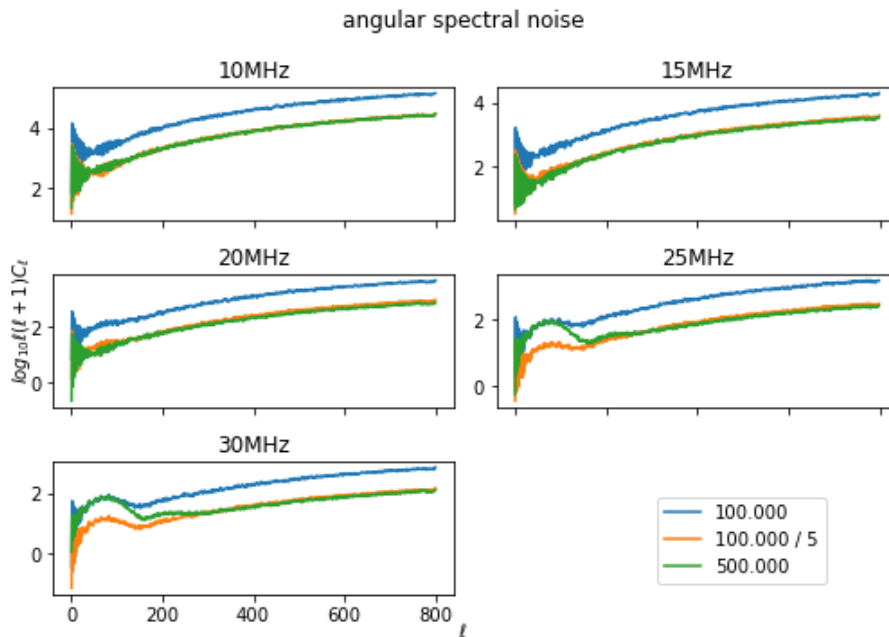


Figure 32: Angular power spectra of the noise for each simulated frequency. the y axis gives the log of the total power present in each mode of ℓ . (in Jansky)

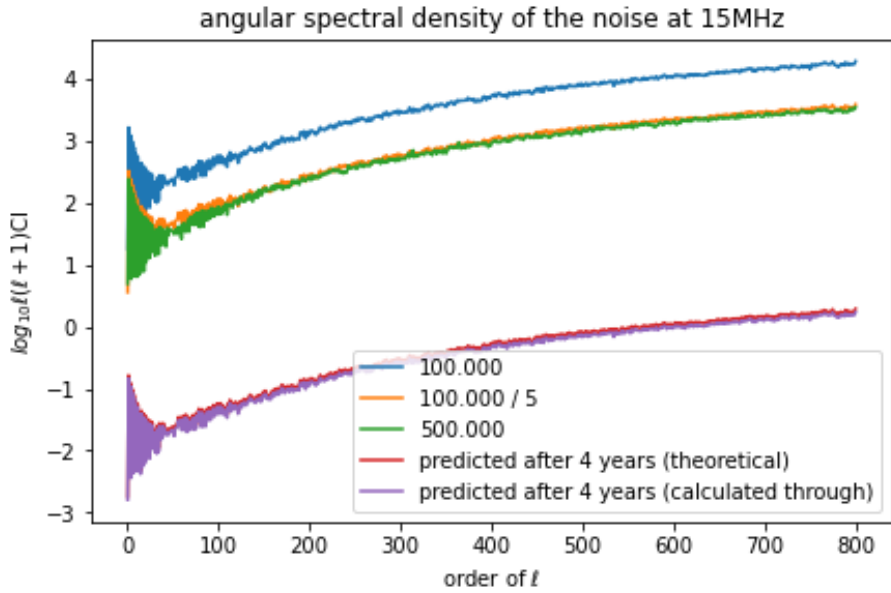


Figure 33: Angular power spectrum taken at 15Mhz. In addition two extra lines are plotted. These lines are the expected reduction of the noise given a larger set of measurements (compared to the 100.000), the noise reduction follows almost exactly the standard square N law for noise reduction.

In addition we see that the noise at large ℓ behaves as a collection of point sources (which of course for the purposes of the simulations, it is), this suggests that the noise at these scales is purely determined by the amount of measurements that can be taken.

To get an idea of the amount of noise that would be expected after a full mission figure 33 plots the expected angular spectrum of the noise after an assumed 4 year mission. These are given in two measures, one using the simple approximation and the other takes into account the overperformance that is displayed between the two simulations.

One of the most interesting reasons to perform a survey at these low frequencies is the 21cm signal obtained from the cosmological dark ages, the 21cm hydrogen spin flip signal from the very early universe (see section 4.3). For this reason figure 35 shows the high estimate of the noise at two frequencies that correspond to certain values for z . We can compare this figure to the one presented in Loeb et al. (figure 34). We can see that the noise for the 30Mhz is at these low values for ℓ is approximately equal or slightly below the predicted values for different cosmological models. higher orders of ℓ cannot be displayed because the resolution of the simulations prohibits these higher orders to be accurately measured. Given the limits however on the resolution of a true image however it should be possible to go up to an order of ℓ in the several thousand. Given that this is a high estimate for the noise level it an encouraging sign that the system could in theory distinguish between different models for cosmological evolution at least for $z \approx 50$ (approximately 30 MHz), higher z values (lower frequencies) have a higher inherent noise so these are unlikely to contain information for the high end orders of ℓ .

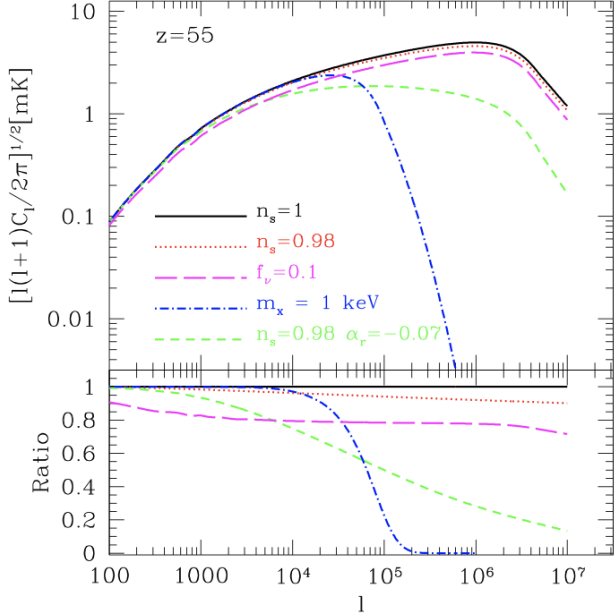


Figure 34: The effect of different models on the predicted anisotropy of the 21cm signal at $z=55$ (approximately 25Mhz). The top panel shows a number of different models and the bottom panel shows the relative fraction between the models. taken from Loeb et al.[19](same as figure 8)

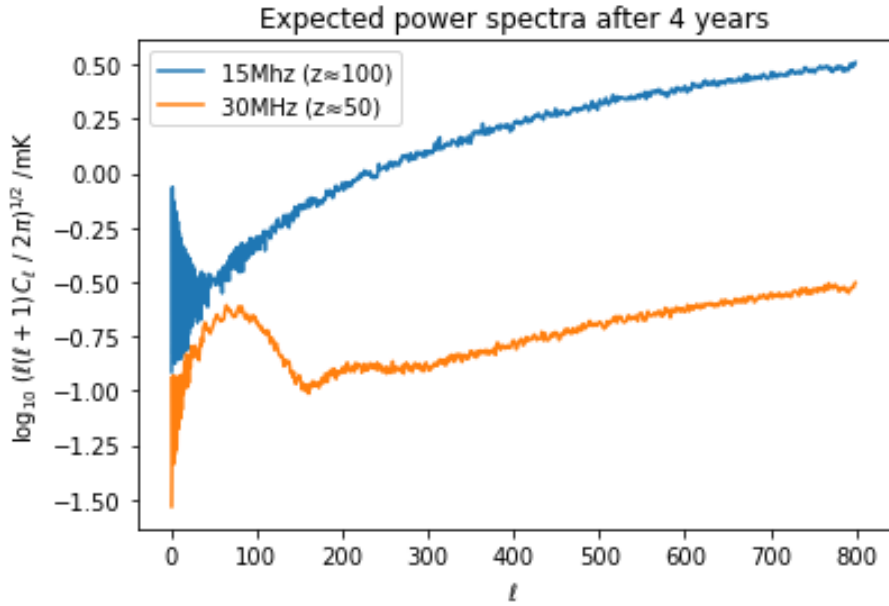


Figure 35: Expectation for the angular spectrum of the noise after a 4 year mission (high estimate) for two values of the 21cm signal. The units on the y axis have been adjusted to match the units in figure8 and figure 34 (mK).

7.3 Cleaned results

The results of the simulations so far have tried to reduce noise effects by adding more measurements in order to improve statistics. Another way to reduce noise that is commonly used in radio astronomy is the CLEAN algorithm. To investigate the effects of such algorithms a simple CLEAN tool was written and used on maps that had significantly less baselines than the full sky maps so far discussed.

The Cleaning algorithm that was used was:

1. Identify the brightest sources in the reconstructed map (in these simulations the 25 brightest points on the map).
2. Build a new map with these brightest sources as point sources at 20% of the identified intensity. (this map is stored)
3. Turn the point source map into a collection of visibilities for all baselines.
4. Subtract the point map visibilities from the original visibilities. (these visibility modifications are also stored)
5. Reconstruct a new map with the modified visibilities. And save this map
6. Repeat with the previously saved map until a predetermined floor for the the intensities has been reached.

In addition to these steps, the same corrections were made on the input model, except the corrections are made on the intensity of the input model (the same pixel is lowered by 20%).

Then the same inspections were performed on these new maps as for the previous maps. This time however the amount of baselines and the resolution of the maps are lower as this process is quite computer time intensive. For this reason the amount of times the routine was run is a maximum of 25 times or when a (modest) floor of 500 Jansky was reached.

figure 36 and 38 show the effects of the cleaning process. With even a modest amount of baselines used (50.000) the manually added sources in the model are already clearly visible in the linear scale after cleaning a modest amount of times. The trade off is of course that the very bright sources are now set to a lower intensity and pop out less, but this is the point of the process and the technique is only useful when not looking at the super bright sources. Figure 39 shows the resulting image made only from the visibilities that the cleaning process removed. This shows a map essentially with only the brightest sources that were present in the original map and shows their (relative to one another's) brightness.

To further investigate the effect on average noise the same procedure as previously on the high baselines maps was done. Figure 38 shows the average noise per pixel in the same scale as they did in the previous section in figure 29. The amount of noise yet again follows the theoretical model very well. If this noise performance is extrapolated to larger measurement sets, it yields a similar system sensitivity as in the previous analysis. The cleaning process is therefore useful for filtering out the stronger sources present but has a negligible effect on the noise present in other sections of the map.

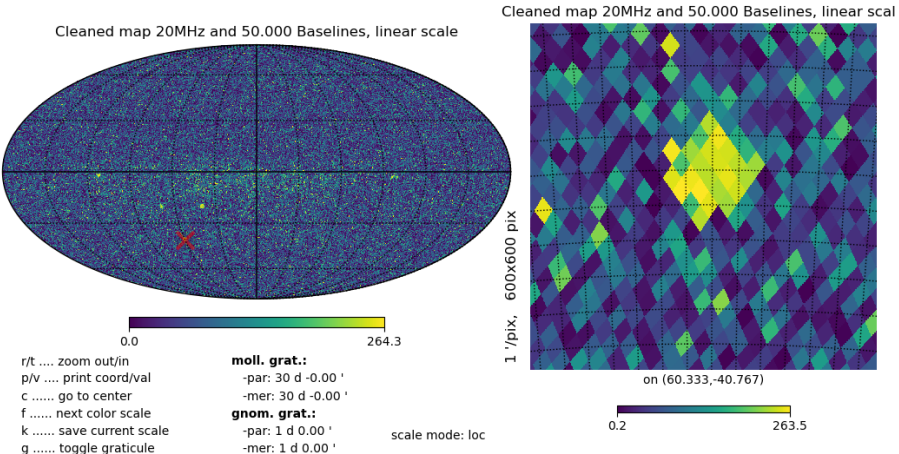


Figure 36: Mollweide view of the full sky map after the cleaning algorithm. The added sources become Visible even on linear scale with a "modest" 50.000 baselines used.

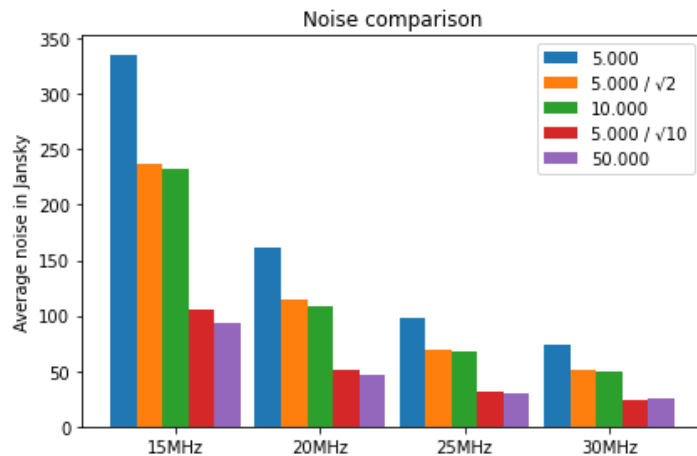


Figure 37: Average noise per pixel in the cleaned map for different baselines and frequencies. (The 10Mhz map turned out to be corrupted and is therefore not displayed)

The angular noise spectrum as presented in figure 40 a similar effect is visible. although there is a slight effect on the higher order terms most of the improvement is in the lower orders. this is consistent with the dampening of the bright sources in the center of the galaxy. This issue as already discussed can likely already be solved by proper calibration of the bright sources in the full sky. Cleaning is therefore unlikely to achieve much with respect to measuring the anisotropy compared to a longer mission lifespan.

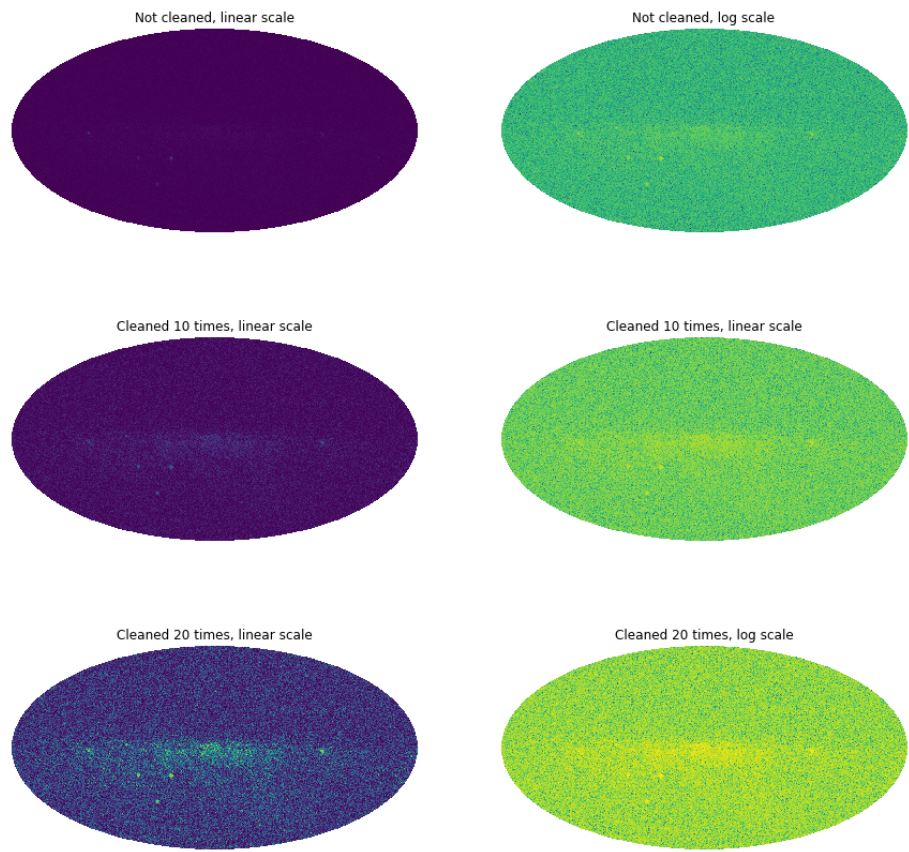


Figure 38: Evolution of the residual image after the cleaning algorithm is run a number of times. the number of cleaning routines ran is 10 times (middle) and 20 times (bottom). After each cleaning routine very bright (and small) sources (the center of the galaxy and background galaxies in the input model) are suppressed allowing weaker sources to be become visible. In the top left image there are two very bright small but very bright spots in the image that drowns out the rest of the present sources.

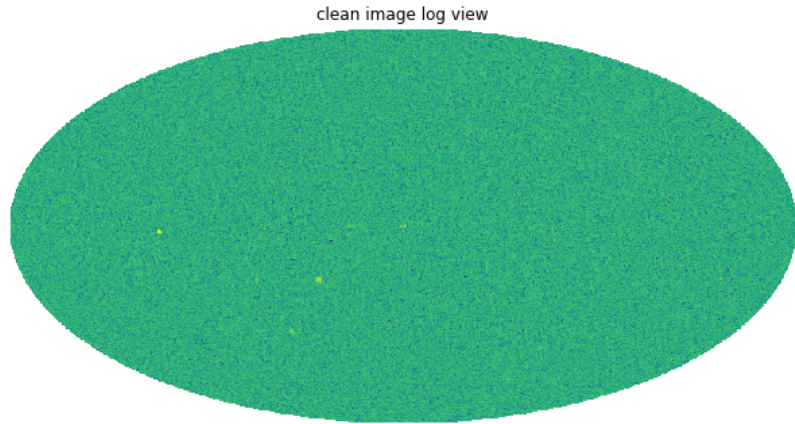


Figure 39: Model image made from the removed visibilities of figure 37 and figure 38. (Linear scale). We can see that the bright source on the left was mostly removed as well as the centre of the galaxy and a little bit from the added sources. This allows an image to be made from only the brightest sources present (up to some floor value specified for the cleaning process).

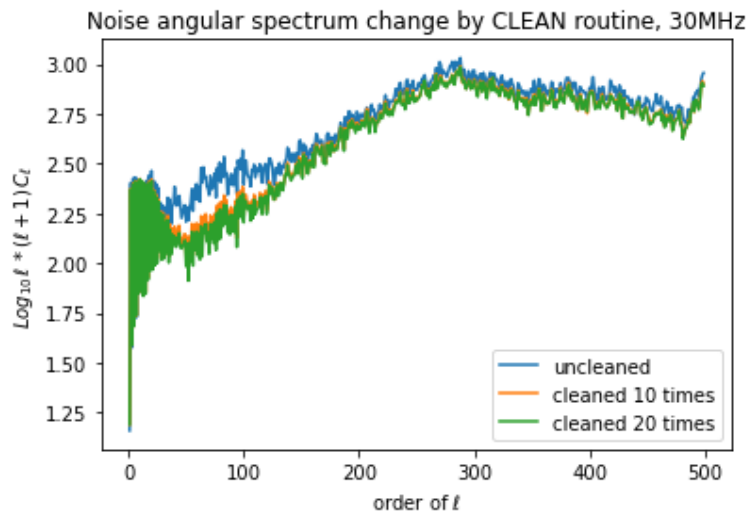


Figure 40: The angular noise spectra after cleaning. the cleaning process appears to not affect the higher orders of ℓ but they do suppress the structure of the signal as expected, which are the contributions from the center of galaxy structures.

8 Requirements

The simulations show that the system can be effective at performing the measurement to fulfil at least some of scientific goals stated. After an assumed mission duration of 4 years we will be able to detect sources fainter than 1 Jansky with an angular resolution below the arcminute scale (depending on frequency), this is however only possible given certain assumptions about the system.

This section presents and discusses some of these requirements that can be distilled from the previous sections. Some of the requirements that can already be distilled from the science cases and the simulations that were done. These are presented here, with more individual explanations in their subsections:

Requirements

Mission duration	4 years	needed for identification of individual sources at 10-15 MHz
Observing bandwidth	0.1 to 50 MHz	inn-system observations peak at 0.5 MHz (SKR, UKR), up to 50 MHz in order to overlap with Earth based observations (LOFAR etc.)
Instantaneous bandwidth	10-20 Mhz	A higher instantaneous bandwidth is preferred but limited by data rates.
Spectral resolution	100 KHz	spectral resolution is mostly important in the very low regime for in-system observations
Antenna Length	≥ 5 meters	Resonance for 5 meters is at 15 MHz
System noise	10% of sky noise	10% is used for the simulation estimates, a lower than this value would either increase accuracy or shorten mission duration
Integration time	≤ 0.1 seconds	Anti-smearing algorithms for lunar orbits (with lower velocities) might be able to extend this
Δv	≥ 400 m/s	Minimum for orbital inclination change plus small reserve
Internal data processing	153-305 Mbit/s	Scales linear with bandwidth, (range is for 10-20 MHz instantaneous bandwidth)
Inter-satellite data link	38-76 Mbit/s	Scales linear with bandwidth, (range is for 10-20 MHz instantaneous bandwidth)
Data link down	3.9-7.8 MBit/s	Scales linear with bandwidth, (range is for 10-20 MHz instantaneous bandwidth)

8.1 Observing bandwidth and resolution

The focus of the system will be the frequency range between 1 and 30 MHz. The lower end of this range (below 10 MHz) would primarily be focused on science within our own solar system or the solar neighborhood (the local interstellar medium). In addition the very low frequencies can be used to measure the direct environment of the Moon which is useful for future lunar based missions.

The higher end of this range (10-30 MHz) would be focused primarily on finding new sources that due to ionospheric interference cannot be easily identified from the Earth's surface.

It is useful in addition to expand the higher end of the frequency range up to 50 MHz. These frequencies are of scientific interest for the cosmological dark ages signal (both the signal itself and its anisotropy). This mission can at these frequencies ranges provide overlap with other missions to measure these signals. In addition these higher frequencies provide some overlap with Earth based low frequency observatories (such as LOFAR) to enable larger spectral characterisation of sources of interest.

For the lower end of the observing bandwidth the lower end should be well below 1 MHz. The expected spectra of electrostatic discharges on the outer planets is expected to have structure between 0.1 and 1 MHz. In a similar fashion the local ISM is expected to yield its structural information between 0.3 and 2 MHz. For these reasons the lower end of the observing bandwidth should be 0.1 MHz.

A larger instantaneous bandwidth will improve system sensitivity over the missions lifespan. Because of the necessary stacking of many measurements the uptime for every frequency (especially the lower ones) becomes an important factor. Thus to improve the quality of the data collected as broad a range of frequencies should be sampled simultaneously.

There is not a compelling argument for this system to have a high resolution within the observing bandwidth of the whole system. The science cases for creating high frequency resolution spectra do certainly exist, such as cosmic ray detection or transient low frequency radio sources, but are only achievable by a system with far more elements. Therefore a modest resolution of 100 KHz for the solar system science is sufficient. For the science cases that are extra-solar, an even more modest 1 MHz of resolution should suffice for the identification of sources such as fossil radio galaxies (it can be argued that an broader bandwidth should suffice since the data on these sources is very limited as of yet).

8.2 Data rate and down-link

The observing data is going to be limited by the amount of data that can be processed on board each of the elements as well as the inter-element and back to Earth communication data rates. The initial data is sampled at nyquist rate of the instantaneous bandwidth, it is then converted by an 8 bit analog to digital converter (or 16 bit if internal datarate is not a limiting factor). This is then downrated to a 2 bit sample. This sample would be locally stored until it can be transmitted to one of the elements that can do the initial processing (likely either the service module element or the surface element). The signals can be correlated for each bin over the integration time from here and sent down to Earth. The data rates needed can be approximated by modifying the approximation made for the OLFAR (orbiting low frequency array) [32]:

$$D_{obs} = 2\Delta\nu N_{bits, raw} \quad (16)$$

$$D_{down} = \frac{2 N_{bins} N_{bits, gain} N_{sats}}{T_{int}} \quad (17)$$

Where D_{obs} is the data stored and transmitted between each of the satellites and the central data processing element (primary node), $\Delta\nu$ is the instantaneous bandwidth, $N_{bits, raw}$ represents the number of bits that are used for the storing of the waveform, $N_{bits, gain}$ is the bit depth after the bit depth processing gain has been applied, N_{sats} is the amount of individual elements that make up the system (assumed to be 3), D_{down} is the data downlink needed for the primary node to transmit back to Earth in total, N_{bins} is the amount of separate bins that the total bandwidth is divided into and T_{int} is the integration time.

Figure 41 shows the dependence of the data that needs to be processed and sent out on the instantaneous bandwidth for an assumed spectral resolution of 100 kHz (number of bins is bandwidth/100 kHz) and 500 kHz. A higher instantaneous bandwidth would be preferred since the lower frequencies would need to be sampled almost continuously. The data transfer rates are well within the bounds of modern data transfer techniques. However it must also be taken into account that the line of sight between the nodes and between the primary node and the Earth is going to be interrupted frequently, thus resulting in higher data transfer rates needed for those periods that line of sight is present.

If the data rate is a limiting factor and the observing frequencies needs to be cut into

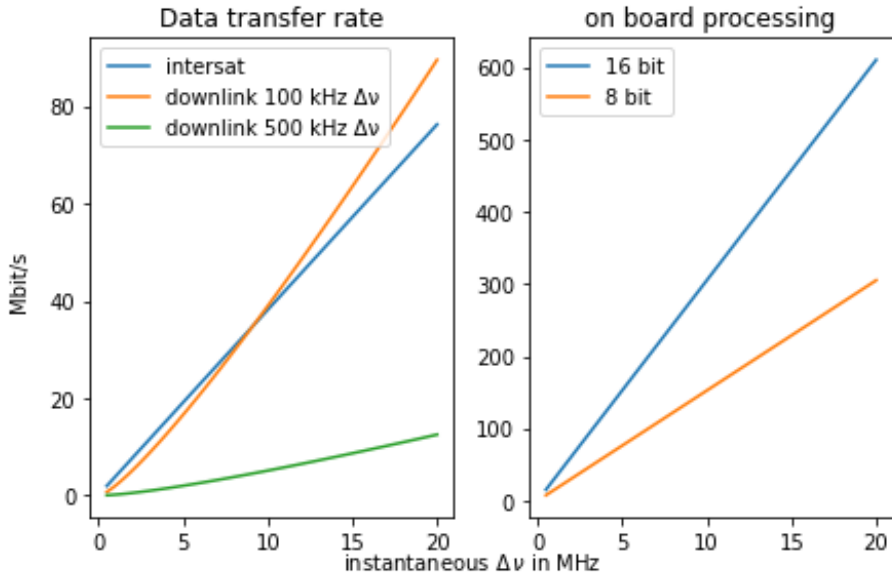


Figure 41: Data processing and linking needed for a set amount of instantaneous bandwidth (assumes 100 or 500 kHz bin size and an integration time of 0.1 seconds). The left figure shows the data rate of each satellite to the central node and the data transfer rate back to Earth for 2 different bit depths. the right figure shows the on board processing needed for both a 8 bit and 16 bit adc.

separate duty cycles greater weight should be placed at the lower end for reasons of noise and of course because these frequencies are harder to measure from Earth and therefore have more to offer from a Lunar orbiting system.

8.3 System noise

The assumption has been made in this work that the system itself only adds a noise factor that is 10% of the noise added by the sky temperature. As stated in Jester et al. [11] the galactic contribution to the noise is so dominant that it is reasonable to ignore all other factors of noise, this thesis however has assumed that some amount of system noise should still be taken into account.

Certainly at the very low frequencies the sky noise is enormous compared to any system noise that is reasonable. But any subtraction of noise in the system from the 10% number can be greatly beneficial to the accuracy of the final images. Therefore a system noise below this 10% should be attempted to be produced. Figure 42 gives a measure of 10% of the sky noise at the frequencies of interest.

8.4 Localization

The validity of the measurements are highly dependent on knowing the relative positions of each element to a high degree of accuracy. Any error in positions would be similar to a higher degree of smearing (discussed in section 3). The requirements would be to know the relative position of each of the orbiting elements to within a fraction of the wavelength (order of meters) [32].

The system would therefore require some way of updating the relative positions in real time. Some of this is alleviated because any orbital changes are slow to materialize

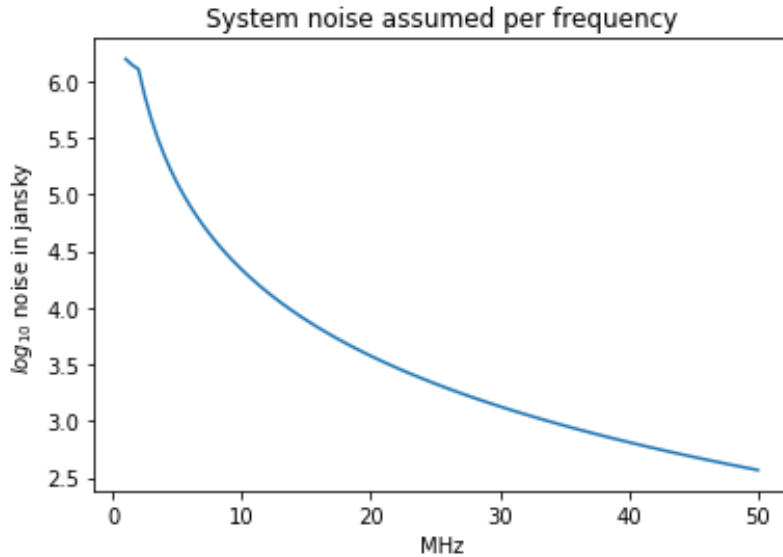


Figure 42: System noise assumed (10 percent of sky rms noise)

compared to the integration time and can thus be modelled given an accurate starting position. In addition since we are only really interested in relative positions this eliminates any structural errors in the position data. The expected position error using modern Lunar Navigation Satellite Systems (LNSS) are expected to be on the order of a meter (though future concepts can get this down to millimeters, likely only for large satellites) [33].

8.5 Antenna length

The frequency range most important for this mission is between the single digit and 30 MHz since these are the frequencies that are hard to measure from the Earth's surface. therefore the centre of the frequency range is around 15 MHz. the antenna would therefore require a length of almost exactly 5 meters in order to have a resonance at this center frequency.

8.6 Δv

In order to perform the orbital inclination change a modest amount of Δv is required to be available to the system. To go from polar orbit to the next frozen orbit requires on the order of 300 m/s. Though some extra on top of this number should be taken in order to overcome any errors that could be introduced as well as stationkeeping plus desaturation of any induced and unwanted rotation. For disposal we can assume only a slight boost into a different inclination would lead to disposal either from the whole Earth-Moon system or a crash onto the lunar surface.

9 Conclusion

The benefits of performing radio interferometry from lunar orbit (and surface) to many areas of interest in astronomy are very clear. A three element system as proposed here can be of value in the exploration of the very low frequency domain that has largely remained unstudied. In addition this system can also function as a pathfinder for future expanded lunar constellations. Although this work specifically assumes a three element system designed for the Chang'e 7 mission statement, the same general setup can be expanded upon and done independently from that specific mission and mission setup. The orbital considerations are valid for any form of a lunar orbiting constellation either released from a main orbiter or injected into orbit separately. The simulations have shown that the data gathered by such a system is sufficient to identify and investigate sources at frequencies that have never been thoroughly investigated. It has also been shown that the noise reduction algorithms can be effective at identifying a larger amount than from the raw data. This allows smaller constellations to be of scientific value in the field of space based radio astronomy.

The software made for this project will provide a useful tool for anyone trying to test the performance for a system with this goal in mind.

The work here still needs to be expanded upon to show long term feasibility (localization and synchronization for example) but it should provide a baseline of requirements that need to be met (and should be doable) in order to successfully explore the lower radio frequencies from lunar orbit and its surface.

10 Suggestions for further work

10.1 Smearing

As discussed in section 3 the relative velocities of the satellites and ground stations can lead to destructive interference in the visibilities. Some schemes have been developed for Earth orbiting satellites to combat this effect [13], these schemes are (relative) velocity dependent and are therefore, given the lower orbital velocities in a lunar orbit compared to an Earth centered orbit, assumed to be even more applicable in this setting. Some study should be done which of the schemes (velocity or direction dependent) would give the best trade-off between lower data volume and high measurement accuracy (see section 3).

10.2 Satellite orientation effects

The simulations that were run for this work were performed under the assumption that the two orbiting elements had a static orientation compared to one another. The surface element was assumed to be rotating in a way that was normal to the surface location chosen. However the effects of rotating satellites on the final sky map has not been simulated. Since the orientation of two dipoles compared to one another can greatly affect the visibilities as well as make it possible to measure different polarizations with a single dipole. The added value or complications of these effects should therefore be investigated further.

10.3 Very low frequency

The simulations that were run and are presented in this work are mostly focused on the high range in the frequency band that is of interest for lunar based radio astronomy. This is done because unfortunately a background emission model does not exist for these lower frequencies (below 10 MHz). This model itself is of course a scientific goal of this mission.

However some of the science cases that have been proposed are more focused on the sub 10 MHz frequencies. These science cases (electrostatic discharges for the outer and inner planets of our own solar system, CME's from the sun, local ISM structure, see section 4) are mostly concerned with the solar system itself or the immediate surroundings.

The problems encountered, most especially the noise inherent to these frequencies, are compounded when looking at even lower frequencies. These frequencies do have scientific value attached to them. Therefore to investigate how the system can best pick up the data relevant to these cases a more in depth simulation should be conducted as these very low frequencies.

10.4 Synchronisation and localization

The accuracy of the measurements taken depend highly on accurate knowledge of positions of the elements, or more accurately the relative positions of the individual elements. For the surface element this is not very hard since the Moon rotates slowly and very predictably.

A method does need to be developed to guarantee a certain accuracy in the localization of the orbiting elements (see section 3.7). Also some research should be performed into the consequences of any inaccuracy that remains.

Similarly the measurement relies on the fact that the measurements taken are taken in the same time interval for each element. A method of synchronization should be explored for this reason.

A good place to start is the idea of a global least squares (GLS) estimator, proposed by Raj Thilak Rajan et al. [34]. They propose a system for use in the Orbiting low frequency array that relies on the two way communication between each node pair. This method is shown to be more reliable than previous methods for both clock synchronization and position data. One of the concerns however is the longer period of nodes being eclipsed by the Moon for longer periods than assumed in their model.

10.5 Calibration

The simulations have shown bright sections of the sky are vulnerable to a higher degree of bad sampling in both a cleaned map and a normal raw one. The system mostly performs an underestimation of these bright sections. Some of this could likely be alleviated by a more robust weighing of the eclipsing parameters but the likely best solutions is to have a scheme for properly calibrating the image. This would likely involve using known emissions in different parts of the sky since the amount of measurements taken have a very high angular dependence.

10.6 Stationkeeping and disposal

Although the choice for a frozen orbit makes sense for a long term mission there would probably need to be some stationkeeping in place for things like orientation. The amount would need to be investigated as well as maybe possibilities for other orbits that may not be frozen entirely but requires only small amount of expended fuel to keep in the target orbit. Another factor is disposal of the elements after the mission duration. Although there are currently no requirements for disposal of lunar orbiting satellites these are likely to be made at some point soon given the increasing interest in Lunar orbitting satellites and missions. Since there is a non zero chance for the satellite to escape the Moon system and end up in a Earth orbit the current regulations might already require disposal to be built in. It would be smart to reserve a small amount of fuel to ensure that at the end of the mission the spacecraft can be disposed of in a responsible manner, either by a lunar surface impact or by putting the craft into an orbit that would escape the Earth-Moon system entirely (though this likely to be more expensive in terms of Δv).

References

- [1] “The Global Exploration Roadmap 2022 ger supplement,” https://www.nasa.gov/sites/default/files/atoms/files/ger-supplement-update-2022-final-10-6-22_tagged.pdf, accessed: 2022-11-25.
- [2] de Gasperin, F., Mevius, M., Rafferty, D. A., Intema, H. T., and Fallows, R. A., “The effect of the ionosphere on ultra-low-frequency radio-interferometric observations,” *A&A*, vol. 615, p. A179, 2018. [Online]. Available: <https://doi.org/10.1051/0004-6361/201833012>
- [3] van Haarlem, M. P., Wise, M. W., Gunst, A. W., Heald, G., McKean, J. P., Hessels, J. W. T., de Bruyn, A. G., Nijboer, R., Swinbank, J., Fallows, R., Brentjens, M., Nelles, A., Beck, R., Falcke, H., Fender, R., Hörandel, J., Koopmans, L. V. E., Mann, G., Miley, G., Röttgering, H., Stappers, B. W., Wijers, R. A. M. J., Zaroubi, S., van den Akker, M., Alexov, A., Anderson, J., Anderson, K., van Ardenne, A., Arts, M., Asgekar, A., Avruch, I. M., Batejat, F., Bähren, L., Bell, M. E., Bell, M. R., van Bemmel, I., Bennema, P., Bentum, M. J., Bernardi, G., Best, P., Bîrzan, L., Bonafede, A., Boonstra, A.-J., Braun, R., Bregman, J., Breitling, F., van de Brink, R. H., Broderick, J., Broekema, P. C., Brouw, W. N., Brüggen, M., Butcher, H. R., van Cappellen, W., Ciardi, B., Coenen, T., Conway, J., Coolen, A., Corstanje, A., Damstra, S., Davies, O., Deller, A. T., Dettmar, R.-J., van Diepen, G., Dijkstra, K., Donker, P., Doorduin, A., Dromer, J., Drost, M., van Duin, A., Eisloffel, J., van Enst, J., Ferrari, C., Frieswijk, W., Gankema, H., Garrett, M. A., de Gasperin, F., Gerbers, M., de Geus, E., Grießmeier, J.-M., Grit, T., Gruppen, P., Hamaker, J. P., Hassall, T., Hoeft, M., Holties, H. A., Horneffer, A., van der Horst, A., van Houwelingen, A., Huijgen, A., Iacobelli, M., Intema, H., Jackson, N., Jelic, V., de Jong, A., Juette, E., Kant, D., Karastergiou, A., Koers, A., Kollen, H., Kondratiev, V. I., Kooistra, E., Koopman, Y., Koster, A., Kuniyoshi, M., Kramer, M., Kuper, G., Lambropoulos, P., Law, C., van Leeuwen, J., Lemaitre, J., Loose, M., Maat, P., Macario, G., Markoff, S., Masters, J., McFadden, R. A., McKay-Bukowski, D., Meijering, H., Meulman, H., Mevius, M., Middelberg, E., Millenaar, R., Miller-Jones, J. C. A., Mohan, R. N., Mol, J. D., Morawietz, J., Morganti, R., Mulcahy, D. D., Mulder, E., Munk, H., Nieuwenhuis, L., van Nieuwpoort, R., Noordam, J. E., Norden, M., Noutsos, A., Offringa, A. R., Olofsson, H., Omar, A., Orrú, E., Overeem, R., Paas, H., Pandey-Pommier, M., Pandey, V. N., Pizzo, R., Polatidis, A., Rafferty, D., Rawlings, S., Reich, W., de Reijer, J.-P., Reitsma, J., Renting, G. A., Riemers, P., Rol, E., Romein, J. W., Roosjen, J., Ruiter, M., Scaife, A., van der Schaaf, K., Scheers, B., Schellart, P., Schoenmakers, A., Schoonderbeek, G., Serylak, M., Shulevski, A., Sluman, J., Smirnov, O., Sobey, C., Spreeuw, H., Steinmetz, M., Sterks, C. G. M., Stiepel, H.-J., Stuurwold, K., Tagger, M., Tang, Y., Tasse, C., Thomas, I., Thoudam, S., Toribio, M. C., van der Tol, B., Usov, O., van Veelen, M., van der Veen, A.-J., ter Veen, S., Verbiest, J. P. W., Vermeulen, R., Vermaas, N., Vocks, C., Vogt, C., de Vos, M., van der Wal, E., van Weeren, R., Weggemans, H., Weltevrede, P., White, S., Wijnholds, S. J., Wilhelmsson, T., Wucknitz, O., Yatawatta, S., Zarka, P., Zensus, A., and van Zwieten, J., “Lofar: The low-frequency array,” *A&A*, vol. 556, p. A2, 2013. [Online]. Available: <https://doi.org/10.1051/0004-6361/201220873>
- [4] NASA. (2022) Chang'e 7 description. Accessed: 2022-11-05. [Online]. Available: <https://nssdc.gsfc.nasa.gov/nmc/display.action?id=CHANG-E-7>

- [5] ——. (2019) Forward to the moon: Nasa’s strategic plan for human exploration. Accessed: 2022-12-05. [Online]. Available: https://www.nasa.gov/sites/default/files/atoms/files/america_to_the_moon_2024_09-16-2019.pdf
- [6] A. Thompson, J. Moran, and G. Swenson, Jr, *Interferometry and Synthesis in Radio Astronomy*, 01 1991, vol. -1.
- [7] J. D. Peterson and W. R. Webber, “Interstellar absorption of the galactic polar low-frequency radio background synchrotron spectrum as an indicator of clumpiness in the warm ionized medium,” *The Astrophysical Journal*, vol. 575, no. 1, pp. 217–224, aug 2002. [Online]. Available: <https://doi.org/10.1086/341258>
- [8] P. Zarka, J.-L. Bougeret, C. Briand, B. Cecconi, H. Falcke, J. Girard, J.-M. Grießmeier, S. Hess, M. Klein-Wolt, A. Konovalenko, L. Lamy, D. Mimoun, and A. Aminaei, “Planetary and exoplanetary low frequency radio observations from the moon,” *Planetary and Space Science*, vol. 74, no. 1, pp. 156–166, 2012, scientific Preparations For Lunar Exploration. [Online]. Available: <https://www.sciencedirect.com/science/article/pii/S0032063312002413>
- [9] M. H. Cohen and W. M. Cronyn, “Scintillation and Apparent Angular Diameter,” , vol. 192, pp. 193–197, Aug. 1974.
- [10] G. Woan, *Capabilities and Limitations of Long Wavelength Observations from Space*. American Geophysical Union (AGU), 2013, pp. 267–276. [Online]. Available: <https://agupubs.onlinelibrary.wiley.com/doi/abs/10.1029/GM119p0267>
- [11] S. Jester and H. Falcke, “Science with a lunar low-frequency array: From the dark ages of the universe to nearby exoplanets,” *New Astronomy Reviews*, vol. 53, no. 1-2, p. 1–26, May 2009. [Online]. Available: <http://dx.doi.org/10.1016/j.newar.2009.02.001>
- [12] G. Woan, “Capabilities and limitations of long wavelength observations from space,” *Geophysical Monograph Series*, 01 2000.
- [13] C. Vertegaal, H. R. Pourshaghghi, S. Wijnholds, and M. Bentum, “Time smearing in space-based 3d synthesis imaging,” in *2022 IEEE Aerospace Conference (AERO)*, 2022, pp. 1–8.
- [14] A. Cohen, “Estimates of the classical confusion limit for the lwa.” 2004. [Online]. Available: <http://www.ece.vt.edu/swe/lwa/memo/lwa0017.pdf>.
- [15] K. M. Blundell and S. Rawlings, “Spectral ageing: a new age perspective,” 2002. [Online]. Available: <https://arxiv.org/abs/astro-ph/0209372>
- [16] Murgia, M., Parma, P., Mack, K.-H., de Ruiter, H. R., Fanti, R., Govoni, F., Tarchi, A., Giacintucci, S., and Markevitch, M., “Dying radio galaxies in clusters,” *A&A*, vol. 526, p. A148, 2011. [Online]. Available: <https://doi.org/10.1051/0004-6361/201015302>
- [17] N. Oozeer, L. Rudnick, M. F. Bietenholz, T. Venturi, K. Knowles, K. Kolokythas, and N. Mhlahlo, “Discovery of rare dying radio galaxies using meerkat,” *Galaxies*, vol. 9, no. 4, 2021. [Online]. Available: <https://www.mdpi.com/2075-4434/9/4/102>
- [18] A. Lewis and A. Challinor, “The 21cm angular-power spectrum from the dark ages,” *Phys. Rev. D*, vol. 76, p. 083005, 2007.

- [19] A. Loeb and M. Zaldarriaga, "Measuring the small-scale power spectrum of cosmic density fluctuations through 21 cm tomography prior to the epoch of structure formation," *Physical Review Letters*, vol. 92, no. 21, may 2004. [Online]. Available: <https://doi.org/10.1103%2Fphysrevlett.92.211301>
- [20] G. Mann, F. Jansen, R. J. MacDowall, M. L. Kaiser, and R. G. Stone, "A heliospheric density model and type III radio bursts," , vol. 348, pp. 614–620, Aug. 1999.
- [21] P. Zarka, "Plasma interactions of exoplanets with their parent stars and associated radio emissions," *Ecole de Goutelas*, pp. 190–, 03 2006.
- [22] T. J. W. Lazio, W. M. Farrell, J. Dietrick, E. Greenlees, E. Hogan, C. P. Jones, and L. A. A. Hennig, "The radiometric bode's law and extrasolar planets," *The Astrophysical Journal*, vol. 612, pp. 511 – 518, 2004.
- [23] K. L. Aplin and G. Fischer, "Lightning detection in planetary atmospheres," *Weather*, vol. 72, no. 2, pp. 46–50, 2017. [Online]. Available: <https://rmets.onlinelibrary.wiley.com/doi/abs/10.1002/wea.2817>
- [24] R. Lorenz, "Lightning detection on venus: a critical review," *Progress in Earth and Planetary Science*, vol. 5, 12 2018.
- [25] J.-M. Grießmeier, P. Zarka, and H. Spreeuw, "Predicting low-frequency radio fluxes of known extrasolar planets," *Astronomy & Astrophysics*, vol. 475, no. 1, p. 359–368, Aug 2007. [Online]. Available: <http://dx.doi.org/10.1051/0004-6361:20077397>
- [26] K. Kumar, J. Melman, E. Iorfida, J. Leolux, and R. Noomen, "Tudat: a modular and robust astrodynamics toolbox," 05 2012.
- [27] A. Elipe and M. Lara, "Frozen orbits about the moon," *Journal of Guidance, Control, and Dynamics*, vol. 26, no. 2, pp. 238–243, 2003. [Online]. Available: <https://doi.org/10.2514/2.5064>
- [28] M. A. Sirwah, D. Tarek, M. Radwan, and A. Ibrahim, "A study of the moderate altitude frozen orbits around the moon," *Results in Physics*, vol. 17, p. 103148, 2020. [Online]. Available: <https://www.sciencedirect.com/science/article/pii/S2211379720306008>
- [29] H. Zheng, M. Tegmark, J. S. Dillon, D. A. Kim, A. Liu, A. R. Neben, J. Jonas, P. Reich, and W. Reich, "An improved model of diffuse galactic radio emission from 10 MHz to 5 THz," , vol. 464, no. 3, pp. 3486–3497, Jan. 2017.
- [30] K. M. Górski, E. Hivon, A. J. Banday, B. D. Wandelt, F. K. Hansen, M. Reinecke, and M. Bartelmann, "HEALPix: A Framework for High-Resolution Discretization and Fast Analysis of Data Distributed on the Sphere," , vol. 622, no. 2, pp. 759–771, Apr. 2005.
- [31] D. M. Smith, M. J. Arts, A.-J. Boonstra, and S. J. Wijnholds, "Characterisation of astronomical antenna for space based low frequency radio telescope," in *2013 IEEE Aerospace Conference*, 2013, pp. 1–9.
- [32] R. T. Rajan, S. Engelen, M. Bentum, and C. Verhoeven, "Orbiting low frequency array for radio astronomy," in *2011 Aerospace Conference*, 2011, pp. 1–11.
- [33] S. Kaplev, M. Titov, T. Valentirova, I. Mozharov, A. Bolkunov, and V. Yaremchuk, "Lunar pnt system concept and simulation results," *Open Astronomy*, vol. 31, no. 1, pp. 110–117, 2022. [Online]. Available: <https://doi.org/10.1515/astro-2022-0014>

- [34] R. T. Rajan and A.-J. Veen, “Joint ranging and clock synchronization for a wireless network,” 12 2011, pp. 297–300.

A Code

the code used for this work can be found at:

<https://github.com/ronaldbouma/Chang-e-7-Simulations>